

TERAHERTZ INTERFEROMETER FOR CHARACTERIZATION
OF THIN FILM SAMPLES

By

SAILAJA KRISHNAMURTHY

Bachelor of Science

University of Madras


Madras, India

1997

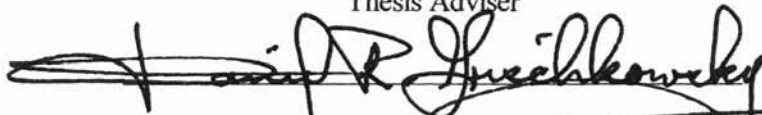
Submitted to the Faculty of the
Graduate College of the
Oklahoma State University
in partial fulfillment of
the requirements for
the Degree of
MASTER OF SCIENCE
August, 2002

TERAHERTZ INTERFEROMETER FOR CHARACTERIZATION
OF THIN FILM SAMPLES

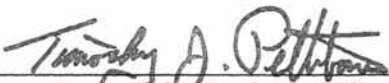
Thesis Approved:



Thesis Adviser



James C. West



Dean of the Graduate College

TABLE OF CONTENTS

Chapter	Page
I. INTRODUCTION -----	1
II. BASIC INTERFEROMETRY -----	4
History -----	4
Classifications -----	5
Applications -----	6
Michelson Interferometer-----	7
Mach-Zehnder Interferometer-----	9
Rayleigh Interferometer -----	10
Sagnac Interferometer-----	11
Fourier Transform Infrared Spectroscopy -----	11
III. THz TIME-DOMAIN SPECTROSCOPY -----	14
Experimental Setup-----	14
Generation and Detection of THz radiation -----	16
THz Transmitter -----	16
THz Receiver -----	17
Limitations for Characterizing Thin Samples-----	18
Noise Treatment -----	18
Lock-in-Amplifier phase -----	18
IV. THz TIME-DOMAIN INTERFEROMETRY -----	21
A. Silicon Prism Configuration-----	21
Experimental Setup-----	21
Mach-Zehnder Configuration-----	21
Michelson Configuration-----	23
Experimental Results-----	26
Theory -----	30
Destructive Interference-----	30
Refractive Index & Absorption Coefficient -----	35
Time-Domain Analysis -----	40

Chapter	Page
B. Retroreflector Configuration -----	43
Experimental Setup-----	43
Experimental Results-----	44
Theory-----	48
Destructive Interference -----	48
Refractive Index & Absorption Coefficient -----	48
V. CONCLUSIONS-----	50
VI. REFERENCES-----	52
APPENDIX-----	56

LIST OF FIGURES

Figure	Page
2-1 Michelson interferometer -----	7
2-2 Mach-Zehnder interferometer -----	9
2-3 Rayleigh interferometer -----	10
2-4 Sagnac interferometer -----	11
3-1 Basic THz-TDS (TeraHertz Time-Domain Spectroscopy) setup-----	14
3-2 THz transmitter chip configuration -----	16
3-3 THz receiver chip configuration -----	17
3-4 Lock-in-amplifier phase component -----	20
3-5 THz signal acquisition using A.C. bias -----	20
4-1 THz interferometer-Mach-Zehnder setup -----	22
4-2 THz interferometer-Michelson setup (double beamsplitters) -----	24
4-3 THz interferometer-Michelson setup (single beamsplitter)-----	25
4-4 Measurements of THz signals (only one arm open) -----	26
4-5 Amplitude spectrum of THz signals (only one arm open) -----	27
4-6 Measurement of THz signal (both arms open) -----	28
4-7 Amplitude spectrum of THz signal (both arms open)-----	28
4-8 Difference between interferometer signals with both arms open-----	29
4-9 Fresnel reflection coefficients at silicon-air and silicon-metal interfaces--	30
4-10 Interference by frequency dependent phase shift -----	34
4-11 Transmission coefficients corresponding to Fabry-Perot oscillations-----	35
4-12 Measurement of refractive index for 2 μ m thick mylar film -----	39

Figure	Page
4-13 Measurement of absorption for 2 μ m thick mylar film -----	39
4-14 Time-domain analysis -----	42
4-15 THz interferometer-retroreflector configuration -----	43
4-16 Measurements of THz signals (retroreflector configuration) -----	45
4-17 Measured interferometer signals with 300nm silicon dioxide film -----	46
4-18 Silicon dioxide growth in silicon wafer-----	47

CHAPTER I

INTRODUCTION

Characterization of materials is one of the enabling roles of optics in modern day industry. Optical instruments such as interferometers and spectrometers are increasingly finding their way from the laboratory to the factory floor in a variety of metrology applications. One of these is the measurement of thin films [1]; the accurate measurement and control of film thickness is critical to applications such as semiconductor processing to food packaging. The non-contact measurement of thin films through well developed optical techniques such as ellipsometry [2] and phase-contrast microscopy [3] relies on the strong wavelength and angle dependence of interference of light from the boundary layers of the film. However these techniques are not applicable for measurement of opaque films.

The recently developed techniques of THz Time Domain Spectroscopy (THz-TDS) [4] and THz tomography [5,6] have been shown to be able to perform measurements on, and images of, samples which are opaque in the visible and near infrared regions of the spectrum. These THz methods have demonstrated non-contact characterization of semiconductors [4], flames [7], and images of water content [6]. In THz-TDS a single cycle electromagnetic pulse with THz bandwidth is used to probe a sample. Changes in the complex amplitude spectrum of the pulse returns information on the refractive index

and absorption of the sample by comparing the change in pulse transmission across bandwidths that can range from 100 GHz to 5 THz. THz-TDS has demonstrated power dynamic ranges of 10^8 , with a well collimated beam that can be propagated over distances of meters. The utility of THz-TDS is limited for certain samples however. In the case the sample is very thin, or with low index and absorption, it is very difficult to distinguish changes in THz pulse caused by the sample from those caused by long term fluctuations in the driving laser source or experiment. Recently such techniques have been extended for thin sample characterization [8]. Using standard THz TDS, 172 μm films of polyimide has been characterized [9]. In transmission measurements, rapid sample dithering has permitted differential measurements of parylene-N films [10]. An interferometer incorporating the Gouy phase shift has permitted reflection measurements of features as small as 12.5 μm [11, 12].

This thesis describes a THz time-domain interferometer which can perform characterization of thin, low absorbance samples with improved accuracy compared to standard THz-TDS. This device utilizes the standard Michelson configuration with a geometry which incorporates a nearly 180° phase shift in one arm to produce destructive interference across over a decade of frequency in the electromagnetic spectrum. This system automatically compensates for changes in the THz signal over the course of a measurement due to slow laser fluctuations. Additionally, under certain conditions this measurement technique yields nearly instantaneous measurements of film thickness with a resolution of under one micron.

Two different configurations of interferometer setups have been developed to achieve the 180° phase shift of one arm relative to the other for destructive interference. The first approach is using high resistivity silicon prisms where total internal reflection of THz pulses provides a nearly 180° phase shift [13]. The second approach is using 90° retroreflectors where polarization of THz pulses provides nearly 180° phase shift.

Two different configurations of interferometer setups have been developed to achieve the 180° phase shift of one arm relative to the other for destructive interference. The first approach is using high resistivity silicon prisms where total internal reflection of THz pulses provides a nearly 180° phase shift [13]. The second approach is using 90° retroreflectors where polarization of THz pulses provides nearly 180° phase shift.

CHAPTER II

BASIC INTERFEROMETRY

Interference occurs when radiation follows more than one path from its source to the point of destination. Interference effects can be observed when two beams with exactly the same wavelength are superposed. Phenomena caused by the interference of light waves can be seen all around us: typical examples include the colors of an oil slick or a thin soap film.

History of Interferometry [14]

The earliest studies of interference are intimately bound up with the evolution of the theories of light propagation.

In 1665 - Grimaldi discovered the diffraction fringes produced by a narrow obstacle and by a slit. He tried to explain the observations of the fringes by supposing light to consist of a fine fluid in a state of vibration.

1678 - Huygens announced the principle of wave propagation through subsidiary wavelets.

1704 - Newton discovered the interference colors of thin films called Newton's rings.

1802 - Young discovered the principle of coherence and principle of superposition, both of which are fundamental to interference.

1809 - Herschel discovered highly sharpened fringes in a thin film when light emerges near grazing incidence.

1815 - Fresnel laid the firm foundation of theory of light propagation and light diffraction [15, 16].

1817 - Brewster reported the interference effect, which takes place when light passes through or is reflected by two similar plane parallel plates slightly inclined to each other.

1837 - Lloyd performed a wavefront division interference experiment using a single mirror.

From the middle of the nineteenth century onwards many new forms of interference were studied and many of these were applied to widely different fields.

Classifications of Interferometry

Two methods are commonly used to obtain two beams from a single source. They are: i) Wavefront division and ii) Amplitude division. In wavefront division, apertures are used to isolate beams from separate portions of the primary wavefront. In some cases, portions of the primary wavefront are used directly as sources to emit secondary waves, which are then brought together for interfering. In amplitude division, two beams are derived from the same portion of the original wavefront, which travel different paths before recombining and interfering. The THz time-domain interferometer is developed based on the amplitude division principle.

Applications of Interferometry [17]

Interferometric applications range through the electromagnetic spectrum from x-rays to radio waves and apply also to acoustical waves and electrons. The interference effects are used to measure wavelengths of light, to measure distances and to investigate spectra. The applications of interference methods include measurements of refractive index of gases, fluid flow, heat transfer, temperature distribution in plasmas, rotation sensing and variation in lengths of the samples.

In recent years, the applications of interferometers are rapidly increasing for many precise and accurate measurements in optical spectroscopy, metrology and radio astronomy. Since the range of interferometric phenomena is extreme, interferometers have the advantage to operate at a broad range of frequencies. In radio astronomy interferometers operate at frequencies as low as 30 MHz. In the infrared regime, interferometers are used from the visible to wavelengths as long as 300 μm where the applications include high-resolution molecular spectroscopy, comparisons of wavelengths and measurements of lengths to the greatest accuracy, astrophysics, optical testing, mechanical gauging and in lasers. The interferometric methods of spectroscopy have been also applied to wavelengths as short as 0.1 nm where the study of crystal and molecular structures by X-rays depend on the interference effects. The principles of interference also apply to the other fields other than electromagnetics, such as in the fields of acoustics and seismology. The following four different interferometer setups

discussed below are used to accomplish some of the applications as mentioned in this section.

Michelson Interferometer

In the Michelson interferometer the beam from the source is divided by the beamsplitter and the same beamsplitter is used to recombine the beams reflected by the mirrors from two arms as shown in figure 2.1. The difference in distance traveled by the beams in two arms is called the optical path difference, δ . This interferometer is easy to set up and align. The two beam paths are well separated and the optical path difference can be varied by translating one of the mirrors in the arms. The application includes the measurements of variations in length of the samples and optical testing [18].

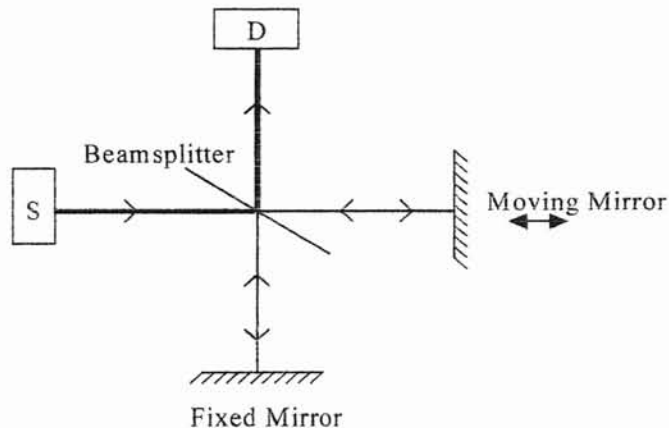


Figure 2.1 Michelson Interferometer, S - Light source, D - Detector

If the moving mirror and fixed mirror are the same distance from the beam splitter, the distance traveled by the two beams that reflect off the mirrors is the same and this condition is called zero path difference (ZPD). The distance that the moving mirror is moved from ZPD is called mirror displacement Δ , and the relationship between mirror displacement and optical path difference is $\delta = 2\Delta$. Let us consider that the source used is monochromatic light with wavelength, λ and the interferometer is at ZPD. When the beams that have reflected off the fixed and moving mirrors recombine at the beamsplitter, they will be in phase. This phenomenon is known as constructive interference. Constructive interference also takes place when the optical path difference is equal to multiples of λ . So constructive interference will take place for any value of δ where the two light beams are in phase which is given by:

$$\delta = n\lambda \quad (2-1)$$

where $n = 0, 1, 2, 3, \dots$

ZPD corresponds to when $n = 0$, and totally constructive interference will take place whenever δ is some multiple of the optical path difference. Let us consider changing the mirror displacement of the interferometer so that the moving mirror is $1/4\lambda$ away from ZPD. Since $\delta = 2\Delta$, the optical path difference is $1/2\lambda$. When the fixed mirror and moving mirror light beams are recombined at the beamsplitter, they will be out of phase. This is known as destructive interference. Destructive interference takes place when the optical path difference is $1/2\lambda$ or some multiple of it. The optical path difference at which totally destructive interference takes place is given by:

$$\delta = (n+1/2)\lambda \quad (2-2)$$

where $n = 0, 1, 2, 3, \dots$

A plot of light intensity versus optical path difference is called an interferogram. All the principles described for Michelson interferometer are applicable to all of the following interferometer designs discussed below.

Mach-Zehnder Interferometer

The Mach-Zehnder interferometer uses two beamsplitters and two mirrors to divide and recombine the beams as shown in figure 2.2. The fringe spacing is controlled by varying the angle between the beams emerging from the interferometer. The two paths are widely separated and are transversed only once and hence the interferometer is relatively difficult to align. The interferometer is widely used for studies of fluid flow, gas flow patterns within research chambers (wind tunnels, shock tubes, etc.), heat transfer and temperature distribution in plasmas [18].

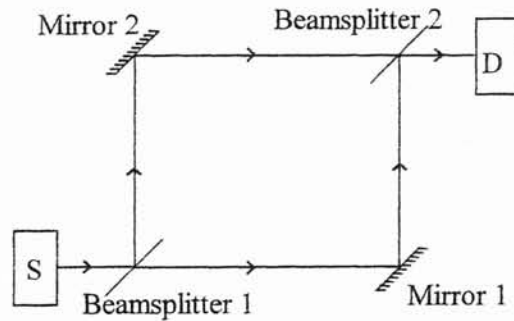


Figure 2.2 Mach-Zehnder Interferometer, S - Light source, D - Detector

Rayleigh Interferometer

The Rayleigh interferometer uses wavefront division to produce two beams from a single source. Two sections from a collimated beam are isolated by a pair of apertures as shown in figure 2.3. Measurements are made on the interference pattern formed on the focal plane. This interferometer has the advantage of simplicity and stability since the two optical paths are equal at the center of the field. The most common applications include measurement of refractive index of gases [18].

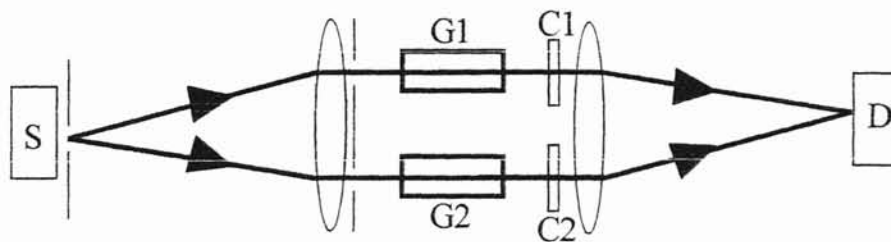


Figure 2.3 Rayleigh Interferometer, S - Light source; D – Detector; G1, G2 - Gas Cells, C1, C2 - Compensators

Sagnac Interferometer

The Sagnac interferometer is a common path interferometer in which two beams traverse the same path in opposite directions as shown in figure 2.4. Since the optical paths traversed by the two beams are nearly equal, fringes can be obtained immediately with an extended white-light source.

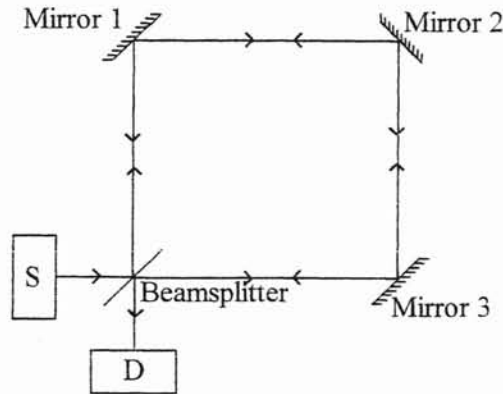


Figure 2.4 Sagnac Interferometer, S - Light source, D – Detector

The interferometer is easy to align and quite stable and one of the applications of this device is its use as a gyroscope. Modified versions of Sagnac interferometer are widely used for rotation sensing [18].

Fourier Transform Infrared Spectroscopy (FTIR) [19]

In a FTIR system, infrared (IR) radiation is introduced to a scanning interferometer and the output radiation intensity as a function of time is decoded into frequency and intensity information through Fourier transformation. So the fundamental measurement obtained by an FTIR is an interferogram, which is Fourier transformed to give a spectrum. The design of most interferometers used in FTIR is based on the two-beam interferometers.

Let us consider monochromatic light of wavelengths λ and 3λ passing through the interferometer as shown in figure 2-1. By substituting 3λ and λ in equations (2-1) and

(2-2) respectively, we get light of this wavelength undergoing constructive interference when $\delta = n\lambda$ and destructive interference when $\delta = 3(n+1/2)\lambda$. So light of wavelengths λ and 3λ undergo totally constructive and destructive interference at different optical path differences and hence the interferograms of the two wavelengths will be different. Each different wavelength of light gives rise to a sinusoidal wave signal of unique frequency that is measured by the detector.

Now let us consider by replacing the monochromatic light source in the interferometer as shown in figure 2-1 with a broadband IR source, as in the case of FTIR. The IR sources give off light at a continuum of wavelengths. The total interferogram measured by the detector is the summation of all the interferograms from all the different IR wavelengths. The measured intensity of light at a given λ is determined by the amplitude of that corresponding wavelengths interferogram. In other words, the interferometer encodes the intensity and wavelength information so all the data can be measured at once, and the Fourier transform decodes the information to obtain the spectrum. Since the intensity information for all the different wavelengths of light are contained in one measured interferogram, there is no need to physically separate the light beam into its component wavelengths and measure intensities one at a time as in dispersive IR spectroscopy. In dispersive IR spectroscopy, a monochromator breaks the light into its component wavelengths, then selects a narrow wavelength range to strike the detector.

The performance of an IR spectrometer is determined by measuring its signal-to-noise ratio (SNR). FTIR is capable of SNRs significantly higher than dispersive spectrometers. The two main advantages are: 1) The throughput of FTIR is based on the

fact that all the IR radiation passes through the sample under study and strikes the detector at once and the detector detects the maximum amount of light at all points during a scan. 2) The FTIR has multiplex advantage, which is based on the fact that all the wavelengths of light are detected at once, and hence can acquire a spectrum much faster than a dispersive instrument. This allows multiple scans of the same sample to be added together. For a constant resolution, the SNR is related to the number of scans (N) added together by: $SNR \propto (N)^{1/2}$.

The applications of FTIR [20] include surface analysis, atomic emission spectrometry, polymer studies, low-temperature studies and biochemical-biomedical studies.

CHAPTER III

THz TIME-DOMAIN SPECTROSCOPY (THz-TDS)

Experimental Setup

In THz-TDS, freely propagating pulses of THz electromagnetic radiation are generated and detected by photoconductively switching the transmitter and receiver with focused femto second laser pulses.

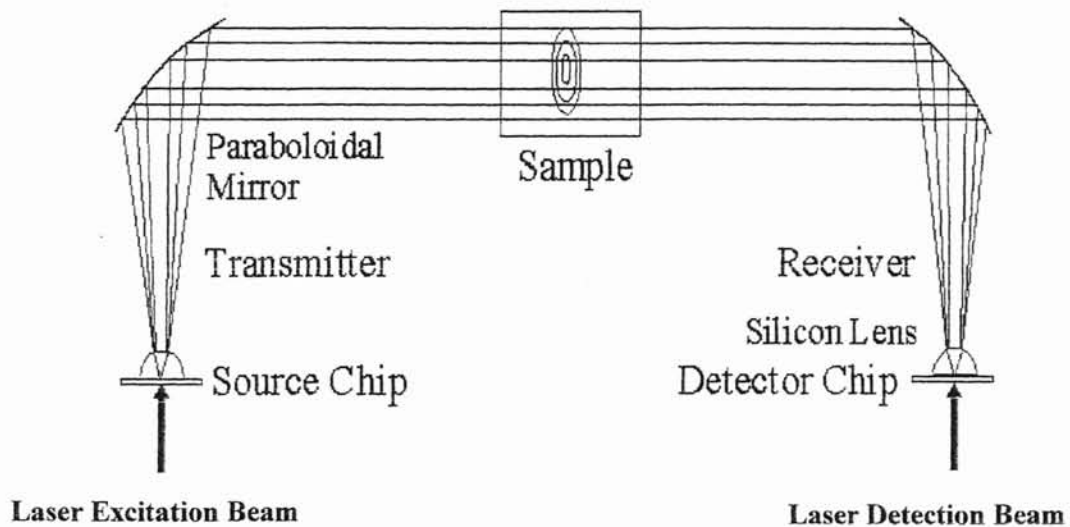


Figure 3-1. Basic THz -TDS Setup

The figure 3-1 shows the experimental set up for the basic THz-TDS system. It consists of a THz source chip, THz detector chip and beam collimating optics. The THz

transmitter generates freely propagating pulses of THz electromagnetic radiation [21]. The radiation emitted is collected by a silicon lens and collimated by a paraboloidal mirror which in turn collimates the THz beam into a highly directional beam. The second paraboloidal mirror focuses the beam back on to the detector chip through the silicon lens. A mechanical chopper modulates the THz signal at approximately 400 Hz and a current amplifier and a lock-in amplifier detect the current proportional to the THz electric field amplitude.

In THz-TDS, a sample with complex refractive index, $n(\omega) = n_r(\omega) - in_i(\omega)$, is placed in the THz beam and the electric field $E_{\text{samp}}(t)$ transmitted through [4], or reflected from [22], the sample is measured. The sample is then removed, and a second, reference scan is measured, $E_{\text{ref}}(t)$. These time dependent data are Fourier transformed numerically to complex amplitude spectra $E_{\text{samp}}(\omega)$ and $E_{\text{ref}}(\omega)$. The ratio of sample spectrum to reference spectrum determines the phase and amplitude shift of the THz pulse interacting with the sample. Assuming a transmitted pulse going through a sample of thickness d :

$$\frac{E_{\text{samp}}(\omega)}{E_{\text{ref}}(\omega)} = \exp\left[-i\frac{\omega}{c}(n_r(\omega) - in_i(\omega) - 1)d\right] \quad (3-1)$$

With the power absorption coefficient given by $\alpha = 2\omega n_i(\omega)/c$, both the real part of the refractive index and absorption spectra are determined from the ratio of the measurements. Dividing the measured complex amplitude spectrum of the pulse propagated through the sample by the spectrum with no sample in place is equivalent to doing a time domain deconvolution of the response of the THz spectrometer from the

measured data. This is complicated in the case of samples with high index since the Fresnel transmission coefficients, $t_{12}(\omega)$ and $t_{21}(\omega)$, on the input and output faces respectively must be included [23].

Generation and Detection of THz radiation

THz Transmitter

Figure 3-2 shows the basic geometry of the THz transmitter 20-80-20 Gallium Arsenide (GaAs) F-chip. The coplanar transmission line structure consists of two 20 μm wide Aluminum lines separated by 80 μm fabricated on an unimplanted high resistivity GaAs substrate.

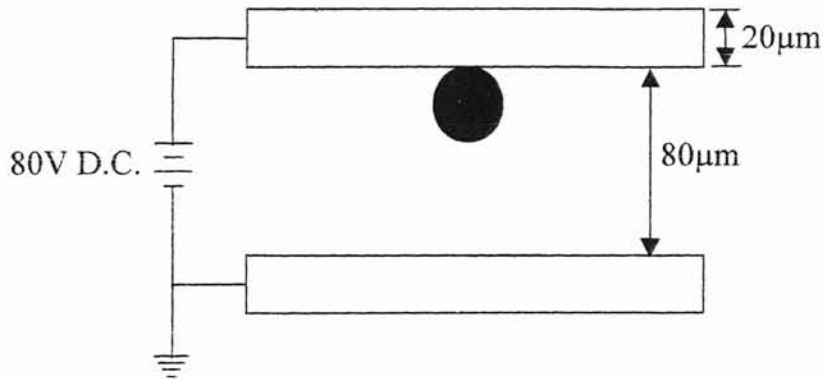


Figure 3-2. THz Transmitter Chip Configuration.

The chip is biased with 80 volts D.C. When the femto second laser pulses are focused on the biased transmission line as shown in the figure 3-2, free carriers are generated and the consequent acceleration of the carriers generates synchronous burst of THz electromagnetic radiation. The THz radiation is emitted into the transmitter chip in

a cone normal to the interface, and is collected and collimated by the silicon lens which is attached to the backside of the chip.

THz Receiver

Figure 3-3 shows the basic geometry of the THz receiver 10-30-10 SOS (silicon on sapphire) B-chip. The coplanar transmission line structure consists of two 10 μm wide Aluminum lines separated by 30 μm fabricated on an ion-implanted SOS substrate.

The THz radiation is focused on to the receiver by the silicon lens attached to the back side of the chip. The electric field of the THz radiation induces a transient bias voltage across the 4.5 μm gap when the gap is focused by the femto second laser pulses. The receiver chip is directly connected to the low noise current amplifier which is connected to the lock-in-amplifier.

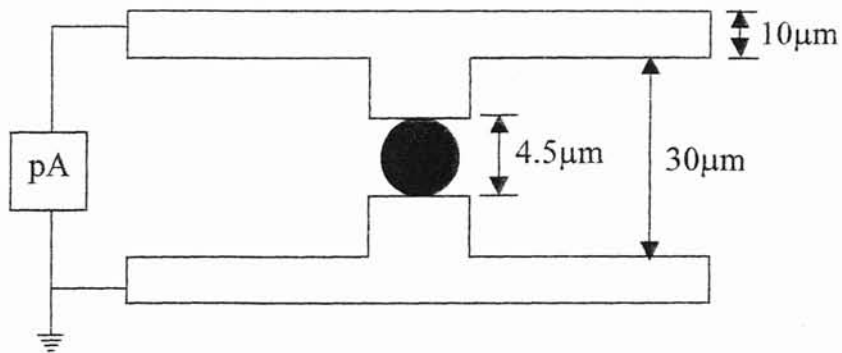


Figure 3-3. THz Receiver Chip Configuration

Limitations for characterizing thin samples

Noise Treatment

The various sources of noise which affect the THz pulse are Laser noise, Chip noise, Chopper noise, 60 Hz noise and Static noise [24,25]. Due to all these fluctuations generated in the THz pulse during the time it takes to acquire two data scans in regular THz-TDS, it is difficult to distinguish changes in the THz pulse caused by the sample in the case of very thin samples.

In THz time domain interferometry, the THz pulse is split into sample and reference pulses and a single measurement gives the superposition of the two pulses. Since changes due to the noise sources and signal drift affect both the pulses simultaneously, the background is eliminated and hence the measured signal is less affected by the time varying fluctuations. So it is possible to characterize thin samples of micron thickness with good precision and accuracy using THz interferometry.

Lock-in-Amplifier Phase

Lock-in-Amplifiers [26] use a technique known as phase-sensitive detection to single out the component of the signal at a specific reference frequency and phase. The reference frequency generated by the mechanical chopper is used to synchronize the reference frequency of the internal oscillator in the lock-in-amplifier to achieve 0° or 180° phase relative to the THz signal detected by the receiver. A lock-in phase

component, $\Phi_{Lock-in}^{\circ}$ will be generated if there is a slight mismatch in the synchronization between the reference frequencies.

For the THz interferometer setup, there is always a phase difference across the finite (~ 1 cm) width of the THz beam due to the optical chopper. For imperfectly aligned beam or spatial rotations or deformations of the beam this phase component contributes to the small error signal in the destructive interference for the interferometer. If the receiver acquires the THz signal at two different positions on the chopper blade slot then there are two different phase components generated in the lock-in amplifier as shown in figure 3-4. I tried the following two different methods to minimize the phase component. First method is, the Thorlabs optical chopper (model MC 1000, chopper blade slot, 0.58 inches) was replaced with Stanford Research Systems optical chopper (model SR 540, chopper blade slot, 1.17 inches). With the larger slot in the chopper blade, the entire THz signal can be made on/off, thus avoiding any chances of clipping the signal and the receiver can acquire THz signal at the same position on the chopper blade. This results in good synchronization between the reference frequencies which in turn minimizes the phase component.

Second method to minimize the lock-in-amplifier phase component is to eliminate the use of mechanical chopper. The transmitter chip was A.C. biased instead of D.C. bias with a High voltage Amplifier [27] as shown in figure 3-5. With A.C. bias we can eliminate the chopper, where the reference frequency to the lock-in-amplifier is generated by the A.C. bias itself. With this configuration, the acquired THz signal is not stable. In spite of all the noise sources present in the system that contribute instability of

the THz signal [24,25], with A.C. bias setup one of the major contributor for noise generation is domestic line voltage.

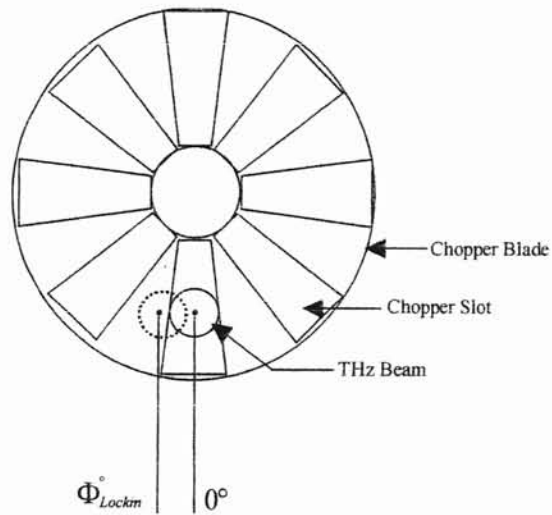


Figure 3-4. Generation of Lock-in amplifier phase component in the chopper blade

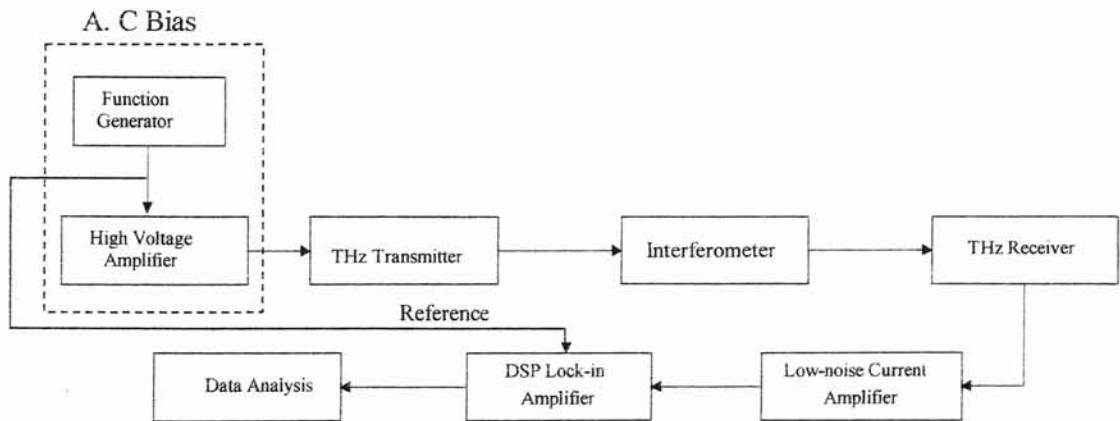


Figure 3-5 Signal Acquisition by A.C. biasing the Transmitter Chip

CHAPTER IV

THz TIME-DOMAIN INTERFEROMETRY

A. Silicon Prism Configurations

Experimental Setup of THz Interferometer

The experimental setup for THz interferometer is developed based on two different amplitude division configurations. One is Mach-Zehnder configuration and the other is Michelson configuration. As mentioned in chapter II, the Mach-Zehnder setup has high efficiency but it is difficult to align the timing between the two arm signals independently, where as with Michelson configuration the efficiency is low but it is easy to align the two signal path lengths because of the independent adjustment of timing between the two arms. Since the requirement of good overlap of two signals is very important to characterize thin samples, the Michelson configuration is preferred.

Mach-Zehnder Configuration

Figure 4-1 shows the experimental setup of the Mach-Zehnder type interferometer configuration inserted in a standard THz-TDS system. The emitted radiation is collected by a silicon lens and collimated by a parabolic mirror. The THz signal (shown by thick lines) is split by a 0.35 mm thick and 2 inches in diameter silicon beam splitter into

reference and sample pulse trains. The two THz pulse trains are incident on silicon right angle prisms ($48 \times 48 \times 67.8$ mm). One face of the sample arm prism is coated with a 60 nm thick layer of aluminum using a thermal evaporator. The purpose of the thin metal layer is to provide reflection with a Fresnel reflection coefficient of magnitude +1, thus causing a phase shift between the metalized and unmetalized prisms. This is discussed further in the theory section later in this thesis. After passing through the prisms, the separate THz pulses are again made coincident by the second beam splitter. A second parabolic mirror collimates the superposition of the two THz pulse trains which are then incident on the $30 \mu\text{m}$ receiver antenna.

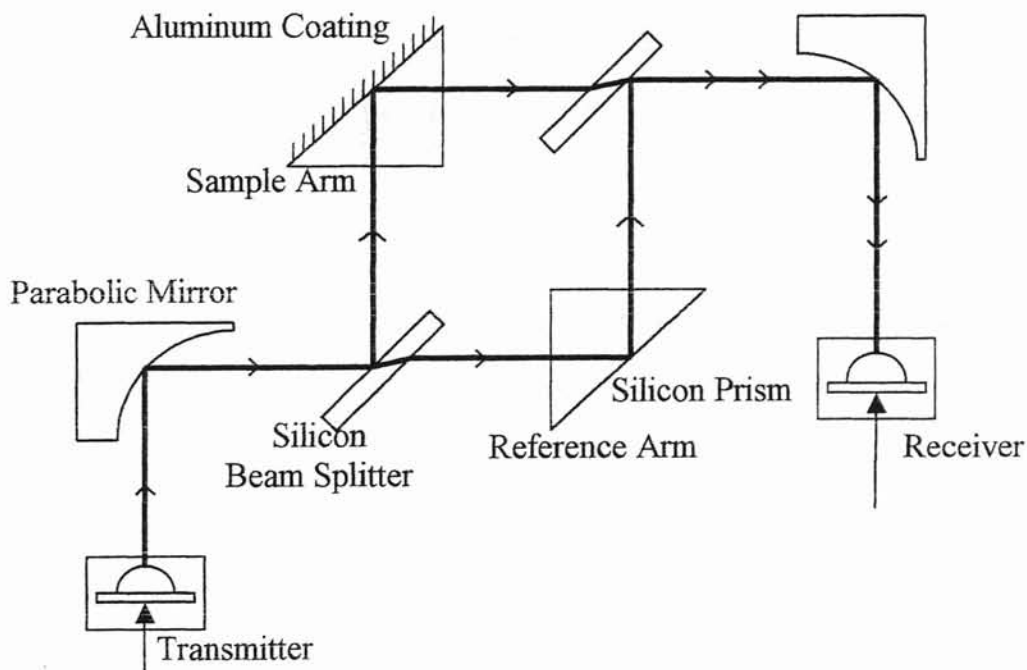


Figure 4-1. THz Interferometer, Silicon Prism Configuration with Mach Zehnder Setup

Michelson Configuration

Figure 4-2 shows the experimental setup of the Michelson type interferometer configuration inserted in a standard THz-TDS system. The emitted radiation is collected by a silicon lens and collimated by a parabolic mirror. The THz signal (shown by thick lines) is split by a silicon beam splitter into reference and sample pulse trains. The two THz pulse trains are incident on silicon right angle prisms which act as roof reflectors. Both the silicon beam splitters and silicon prisms have the same dimensions as stated in Mach-Zehnder setup. One face of the sample arm prism is coated with a 60 nm thick layer of aluminum using a thermal evaporator.. After passing through the prisms, the separate THz pulses are again made coincident by the second beam splitter. A second parabolic mirror collimates the superposition of the two THz pulse trains which are then incident on the 30 μm receiver antenna. Thin film samples are placed in the sample arm in the position shown in figure 4-2. For thin films on substrates, an identical substrate may be used in the reference arm.

The two silicon beamsplitters are used to provide independent position and angle control of the reference and sample arm THz beams to permit the THz beams to be made coincident at the receiver. Both beamsplitters are mounted on standard kinematic mirror mounts. This permits angular control of the reference arm beam in the horizontal (plane of page) and vertical directions (out of page) by the first beamsplitter. The reference arm prism can be translated horizontally to provide independent position control, and the prism is mounted on a tilt table to enable a second vertical tilt adjustment. Similar controls in the sample arm permit full position and angle control of both beams

independently to achieve maximum overlap at the receiver. Additionally the reference arm prism can be translated along the direction of propagation of the THz beam to ensure both arms have identical path length. The prisms are aligned such that the beam is normal to the interface ($\theta_2 = 0^\circ$ and $\phi_2 = 0^\circ$) by rotating the prism such that the propagation time is minimized.

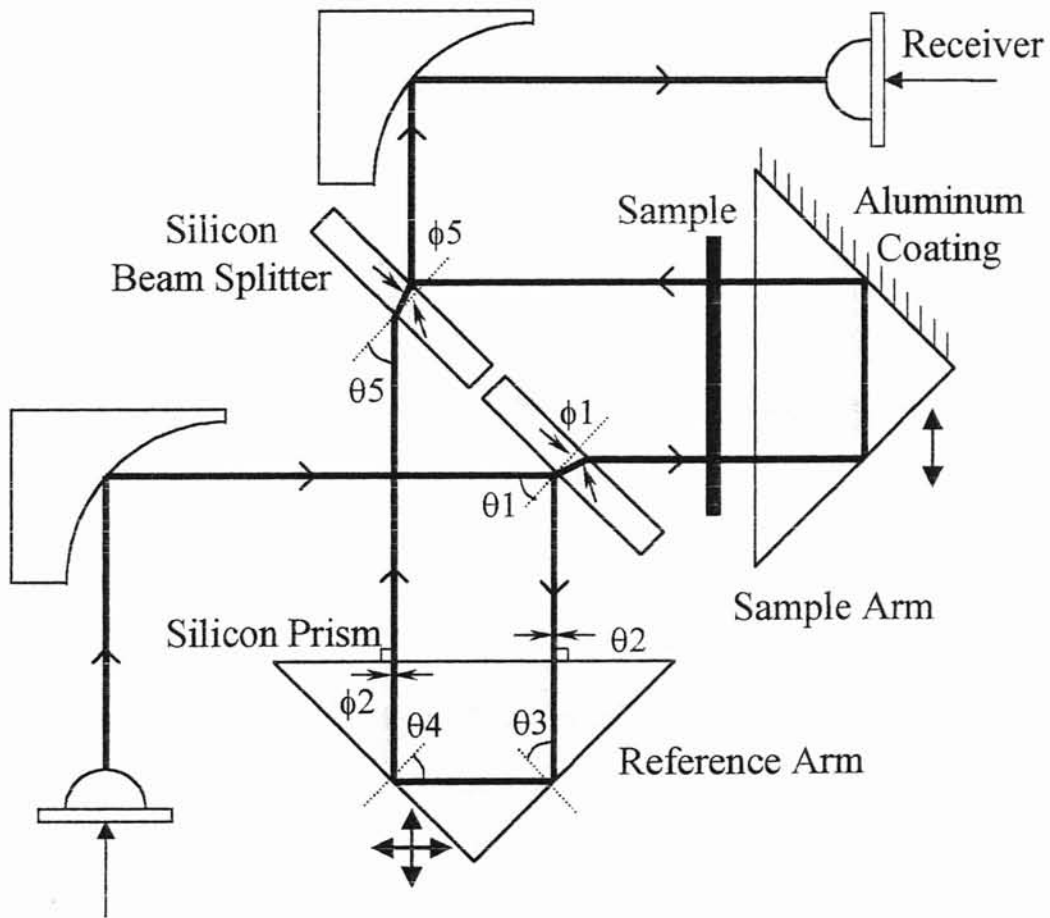


Figure 4-2. THz Interferometer, Silicon Prism Configuration with Michelson Setup

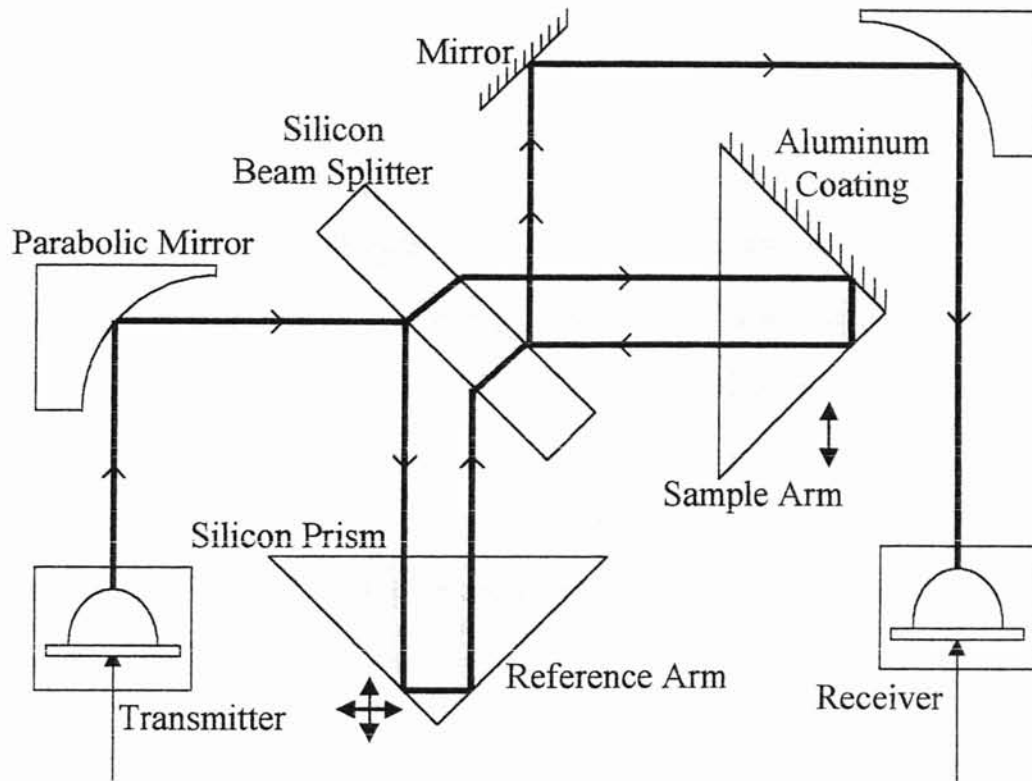


Figure 4-3 THz interferometer Michelson setup with single Beamsplitter

Instead of two beamsplitters in figure 4-2, a single beamsplitter (1cm thick and 3 inches in diameter) is used as shown in figure 4-3. Because of the larger diameter there is no possibility of clipping of the THz signals in both the arms. Since there is no independent angle control of the beams, the two beamsplitters configuration is preferred for the maximum overlap of the signals.

Experimental Results

The measured pulses in the reference arm, $E_{\text{ref}}(t)$, shown by dashed line, and sample arm, $E_{\text{samp}}(t)$, shown by solid line obtained by blocking one arm and measuring the signal in the other arm are shown in figure 4-4. The nearly 180° phase shift of the sample arm relative to the reference arm is clearly seen. The measured signal (points) in the sample arm is also shown when a $2\ \mu\text{m}$ thick Mylar® sample is placed in this arm. The small value of $k_0(n-1)d$ makes these two THz pulses nearly indistinguishable. Figure 4-5 shows the amplitude spectrum of the reference and sample signals which covers a bandwidth of 0.3 to 2 THz

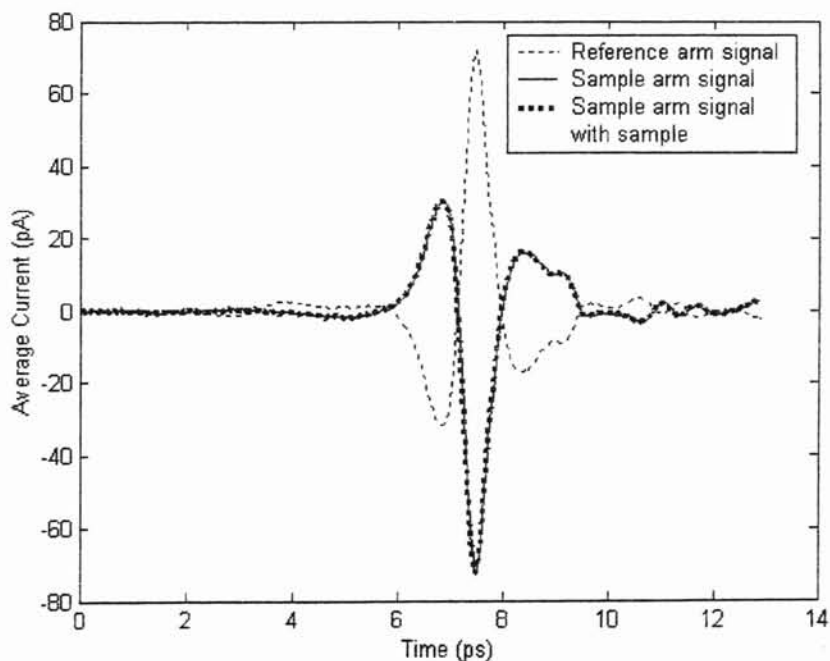


Figure 4-4. Measurements of the THz interferometer signals with only one arm open

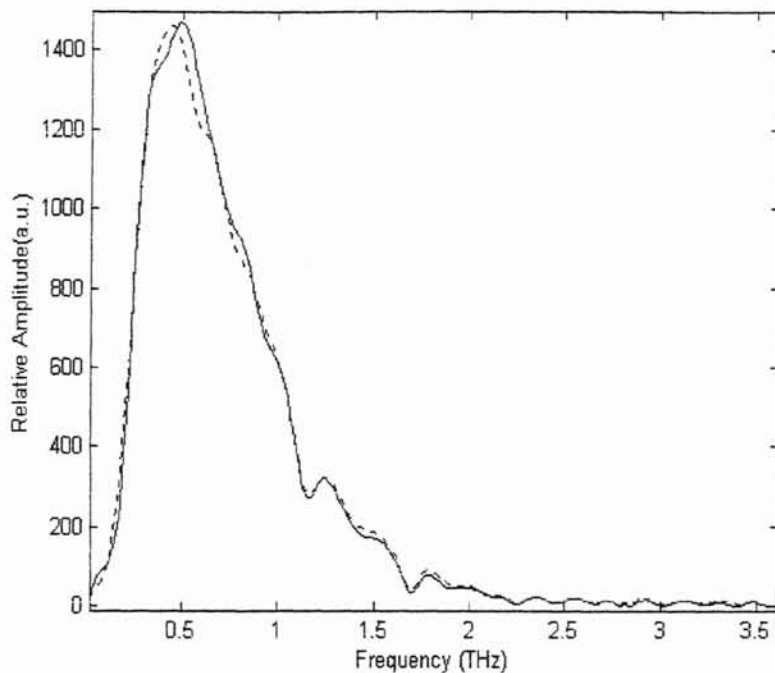


Figure 4-5 Amplitude spectrum for the reference and sample arm signals shown in figure 4-3.

Figure 4-6 shows the measured interferometer signal with both sample and reference arms open, $E_{\phi}(t)$. The solid line corresponds to no sample in either sample or reference arms. The signal measured with both arms open and a nominally 2 μm Mylar film as a sample, $E_{\text{meas}}(t)$, is shown by the dashed line. The amplitude spectrum for $E_{\phi}(t)$ is shown in figure 4-7. Figure 4-8 shows the difference between the interferometer signals with both arms open for the measured data shown in the figure 4-6.

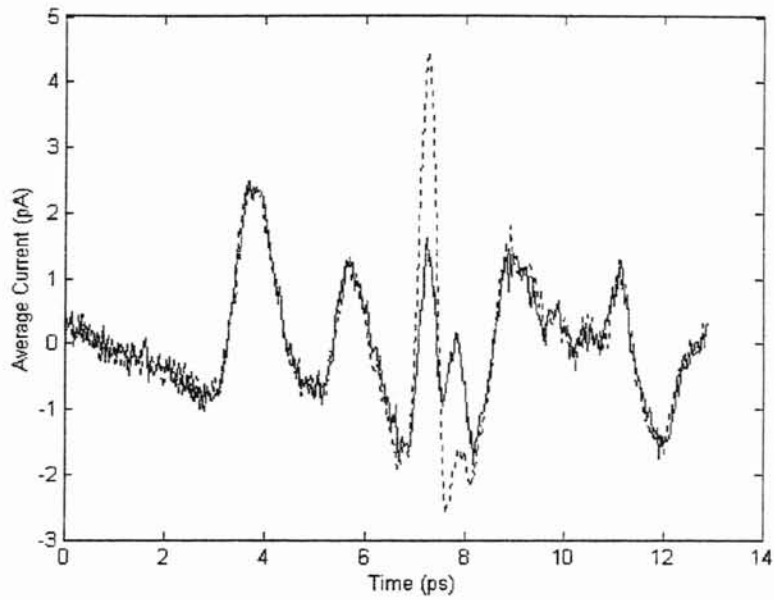


Figure 4-6 Measured interferometer signals with both sample and reference arms open, solid line - without sample, dashed line – with 2 μm thick Mylar film as a sample

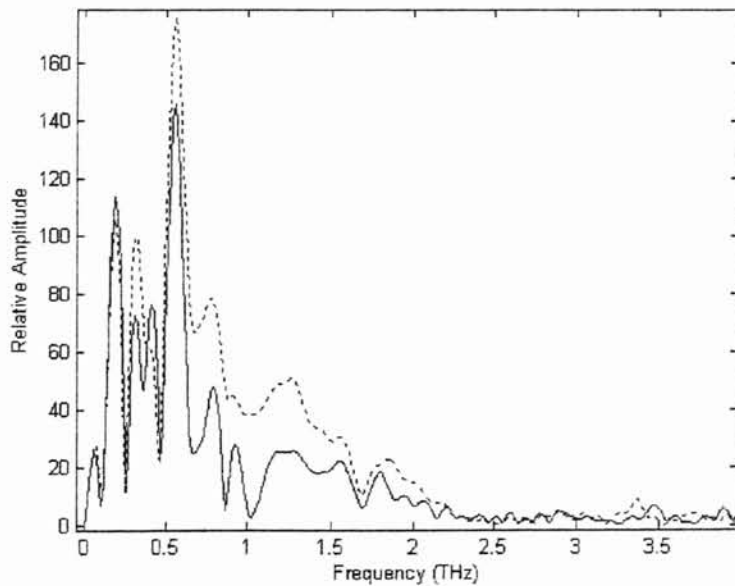


Figure 4-7 The amplitude spectrum for interferometer signal with both sample and reference arms open solid line - without mylar film, dashed line – with mylar film

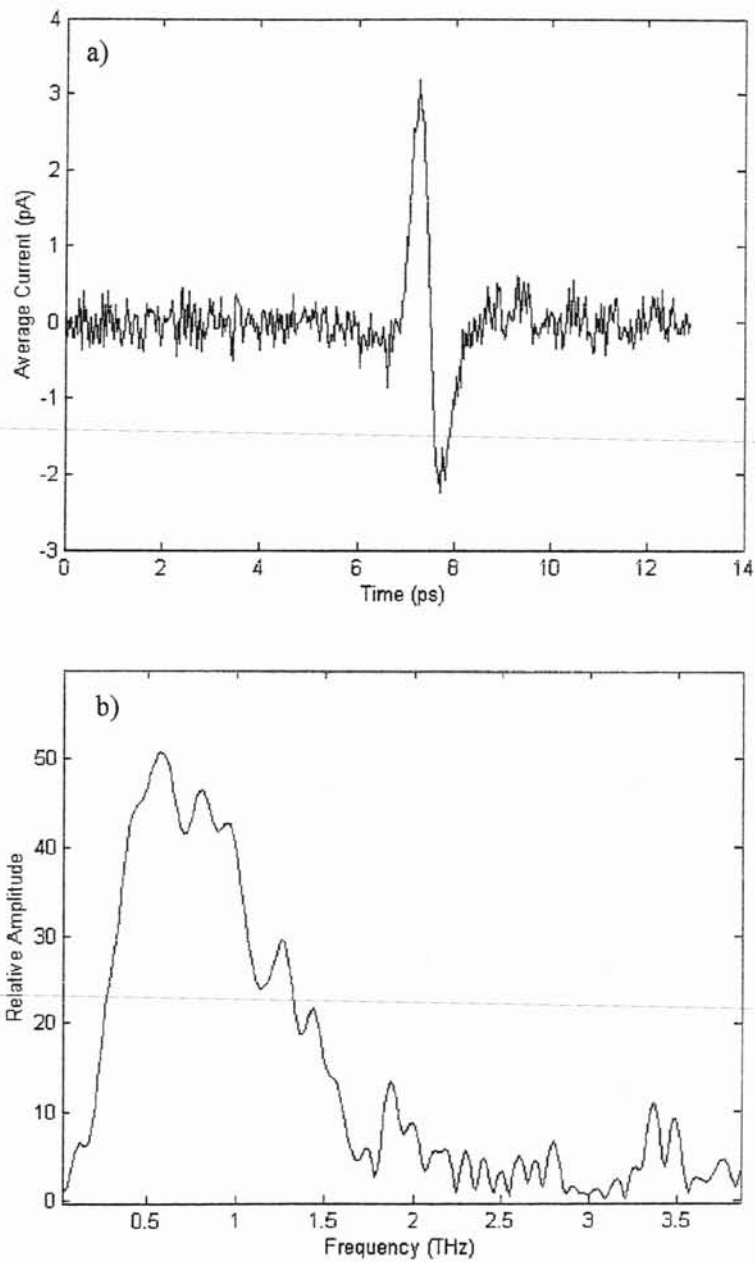


Figure 4-8 Difference between the interferometer signals with both arms open for the measured data shown in the figure 4-6. a) Time-domain data, b) Amplitude Spectrum

Theory

Destructive Interference

In the interferometer pictured in figure 4-8, the THz pulse is split into both sample, $E_{\text{samp}}(t)$, and reference $E_{\text{ref}}(t)$, pulses and a single measurement returns $E(t) = E_{\text{samp}}(t) + E_{\text{ref}}(t)$. This is converted to the frequency domain by taking numerical Fourier transforms of the time dependent field amplitudes. Propagation effects of the beam, and the frequency dependent beam size are ignored in first approximation since the path length is the same for both arms.

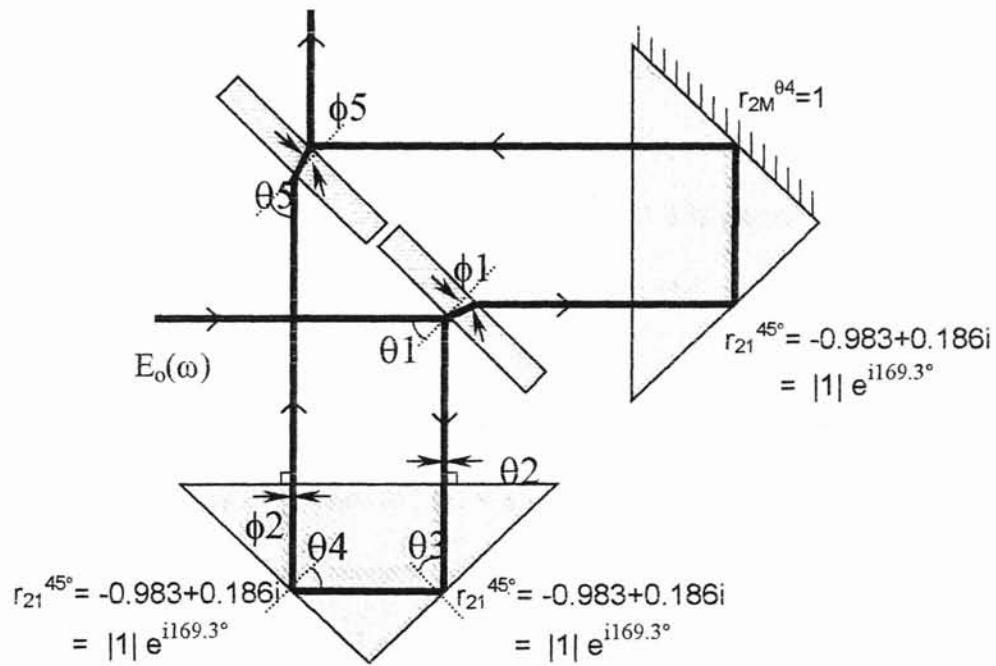


Figure 4-9. Fresnel Reflection Coefficients at Silicon-Air and Silicon-Metal Interfaces.

The frequency dependent fields are given by the field input into each arm, $E_o(\omega)$, modified by the Fresnel transmission and reflection coefficients at each interface for the angles shown in figure 4-9. The measured fields from each arm are then given by the incident field multiplied by the fresnel coefficients along the beam path. These are :

$$\begin{aligned} E_{\text{ref}}(\omega) &= E_o(\omega) r_{12}^{\theta_1} t_{12}^{\theta_2} r_{21}^{\theta_3} r_{21}^{\theta_4} t_{21}^{\phi_2} t_{12}^{\theta_5} t_{21}^{\phi_5} \\ E_{\text{samp}}(\omega) &= E_o(\omega) t_{12}^{\theta_1} t_{21}^{\phi_1} t_{12}^{\theta_2} r_{21}^{\theta_3} r_{2M}^{\theta_4} t_{21}^{\phi_2} t_{12}^{\theta_5} T_s(\omega)^2 \end{aligned} \quad (4-1)$$

for the reference and sample arms where the fresnel coefficients are defined as r_{12}^{θ} for reflection and t_{12}^{θ} for transmission where the subscript “12” corresponds to an air-silicon interface and “21” to a silicon-air interface at incident angle θ . The Fresnel coefficients are given by the following equation [28]:

$$r_{12}^{\theta} = \frac{n_1(\omega)\cos\theta - n_2(\omega)\cos\phi}{n_1(\omega)\cos\theta + n_2(\omega)\cos\phi}; \quad t_{12}^{\theta} = \frac{2n_1(\omega)\cos\theta}{n_1(\omega)\cos\theta + n_2(\omega)\cos\phi} \quad (4-2)$$

where $n_1(\omega)$ is the index of the medium on the incident side of the interface, $n_2(\omega)$ is the index on the transmitted side, and the transmitted angle ϕ is related to the input angle θ by Snell’s Law. The Fresnel coefficient $r_{2M}^{\theta_4}$ in equation (4-1) is the reflection coefficient at the silicon-metal interface. By rotating the prisms to minimize the time delay, the interferometer is aligned so $\theta_3 = 45^\circ$ and $\theta_2 = \phi_2 = 0^\circ$. Under this optimal alignment condition with angles $\theta_1 = \theta_5 = 45^\circ$, $\phi_1 = \phi_5 = 11.9^\circ$, and $n_1 = 1$ and $n_2 = 3.42$ the Fresnel coefficients in equation (4-2) become $t_{12}^{0^\circ} = 0.453$, $t_{21}^{0^\circ} = 1.548$, $t_{12}^{45^\circ} = 0.416$, $t_{21}^{12^\circ} = 1.971$, $r_{12}^{45^\circ} = 0.424$, and $r_{21}^{45^\circ} = -0.983 + 0.186i$.

Contrary to intuition, the silicon-metal reflection, $r_{2M}^{\theta_4}$, has a value of +1 when the field is polarized in the plane of incidence (P) [28]. The plane of incidence is defined as the plane containing the normal to the boundary and the direction of propagation of the

The frequency dependent fields are given by the field input into each arm, $E_o(\omega)$, modified by the Fresnel transmission and reflection coefficients at each interface for the angles shown in figure 4-9. The measured fields from each arm are then given by the incident field multiplied by the fresnel coefficients along the beam path. These are :

$$\begin{aligned} E_{\text{ref}}(\omega) &= E_o(\omega) r_{12}^{\theta_1} t_{12}^{\theta_2} r_{21}^{\theta_3} r_{2M}^{\theta_4} t_{21}^{\phi_2} t_{12}^{\theta_5} t_{21}^{\phi_5} \\ E_{\text{samp}}(\omega) &= E_o(\omega) t_{12}^{\theta_1} t_{21}^{\phi_1} t_{12}^{\theta_2} r_{21}^{\theta_3} r_{2M}^{\theta_4} t_{21}^{\phi_2} r_{12}^{\theta_5} T_s(\omega)^2 \end{aligned} \quad (4-1)$$

for the reference and sample arms where the fresnel coefficients are defined as r_{12}^{θ} for reflection and t_{12}^{θ} for transmission where the subscript “12” corresponds to an air-silicon interface and “21” to a silicon-air interface at incident angle θ . The Fresnel coefficients are given by the following equation [28]:

$$r_{12}^{\theta} = \frac{n_1(\omega)\cos\theta - n_2(\omega)\cos\phi}{n_1(\omega)\cos\theta + n_2(\omega)\cos\phi}; \quad t_{12}^{\theta} = \frac{2n_1(\omega)\cos\theta}{n_1(\omega)\cos\theta + n_2(\omega)\cos\phi} \quad (4-2)$$

where $n_1(\omega)$ is the index of the medium on the incident side of the interface, $n_2(\omega)$ is the index on the transmitted side, and the transmitted angle ϕ is related to the input angle θ by Snell’s Law. The Fresnel coefficient $r_{2M}^{\theta_4}$ in equation (4-1) is the reflection coefficient at the silicon-metal interface. By rotating the prisms to minimize the time delay, the interferometer is aligned so $\theta_3 = 45^\circ$ and $\theta_2 = \phi_2 = 0^\circ$. Under this optimal alignment condition with angles $\theta_1 = \theta_5 = 45^\circ$, $\phi_1 = \phi_5 = 11.9^\circ$, and $n_1 = 1$ and $n_2 = 3.42$ the Fresnel coefficients in equation (4-2) become $t_{12}^{0^\circ} = 0.453$, $t_{21}^{0^\circ} = 1.548$, $t_{12}^{45^\circ} = 0.416$, $t_{21}^{12^\circ} = 1.971$, $r_{12}^{45^\circ} = 0.424$, and $r_{21}^{45^\circ} = -0.983 + 0.186i$.

Contrary to intuition, the silicon-metal reflection, $r_{2M}^{\theta_4}$, has a value of +1 when the field is polarized in the plane of incidence (P) [28]. The plane of incidence is defined as the plane containing the normal to the boundary and the direction of propagation of the

incident wave. When the electric field is parallel to the plane of incidence, the polarization of the wave is referred to as parallel polarization (P) and when the electric field is perpendicular to the plane of incidence, the polarization of the wave is referred to as perpendicular polarization (S). Since the silicon-metal reflection, r_{2M}^{04} , assumes a perfect reflection it is important for the retroreflector configuration which is discussed later.

The complex coefficient $r_{21}^{45^\circ} = -0.983 + 0.186i$ corresponds to total internal reflection with $|r_{21}^{45^\circ}| = 1$ with a phase angle of 169.3° . The electric fields from the reference and sample arms are then:

$$\begin{aligned} E_{\text{ref}}(\omega) &= (0.2266 - i0.0891)E_o(\omega) \text{ and} \\ E_{\text{samp}}(\omega) &= (-0.2392 + 0.0453i)E_o(\omega). \end{aligned} \quad (4-3)$$

The sample transmission function, $T_s(\omega)$ is given by: [28]

$$T_s(\omega) = t_{1S}t_{S1} \exp\left[-i\frac{\omega}{c}(n_r(\omega) - 1 - in_i(\omega))d\right] \quad (4-4)$$

where t_{1S} and t_{S1} are the Fresnel coefficients for $\theta = 0^\circ$ and we assume the sample index is small so secondary reflections can be ignored. Secondary reflections appear later in time and hence are gated out while acquiring the data scans.

Equation (4-3) can be written as:

$$\begin{aligned} E_{\text{ref}}(\omega) &= 0.24\exp(-21.4^\circ)E_o(\omega) \text{ and} \\ E_{\text{samp}}(\omega) &= 0.24\exp(169.3^\circ)E_o(\omega). \end{aligned} \quad (4-5)$$

A phase shift of 180° is required between reference and sample signals in order to get total destructive interference between the two signals. But it is clearly seen that a phase shift of $\Delta\theta = 10.7^\circ$ is present between the two signals. This phase shift arises from the

frequency independent fresnel reflection coefficient which is a complex value for total internal reflection. By choosing large index difference between interface media the phase shift term, $\Delta\theta$ can be minimized. With no sample in the interferometer, the reference arm phase is defined to be 0° . In this case, $T_s(\omega) = 1$, $E_{\text{ref}}(\omega) = 0.24E_o(\omega)$ and $E_{\text{samp}}(\omega) = 0.24\exp(-i169.3^\circ)E_o(\omega)$, which is written $E_{\text{samp}}(\omega) = -0.24\exp(i10.7^\circ)E_o(\omega)$. The temporal phase shift has been observed previously with THz pulses [29].

The measured peak to peak signal in the interferometer with both reference and sample arms open is 3.5% of the difference between the peaks of the reference and sample arms measured individually. A numerical analysis for this system done by varying the beamsplitter and prism angles, and the relative length of each arm, shows that the best extinction possible in the time domain is approximately 2.5% of the signal propagated by one arm. The slight additional signal over the 2.5% calculated minimum is attributed to slight misalignments of the THz beam.

Due to this constant and frequency independent phase shift between the arms, even under optimal alignment conditions complete destructive interference of the THz waveforms is impossible to achieve. It is not possible to adjust the length of one arm an amount Δz relative to the other to achieve destructive interference as could be done in a Michelson interferometer for CW radiation since this causes a frequency dependent phase shift $\exp(-i\omega\Delta z/c)$ which would achieve destructive interference at a discrete number of wavelengths rather than over the entire THz pulse spectrum.

This concept is illustrated in figure 4-10. A reference spectrum shown by (dashed lines) is generated numerically, which covers a bandwidth of approximately 0-10 THz.

A sample spectrum is generated by adding a frequency dependent phase shift $\exp(-i\omega\Delta z/c)$ to the reference spectrum where $\Delta z = 0.3$ mm. Both the reference and sample spectrums are added together to achieve the interference, which is shown by the solid line. It is clearly seen that, we get interference at a discrete number of wavelengths rather than over the entire THz pulse spectrum.

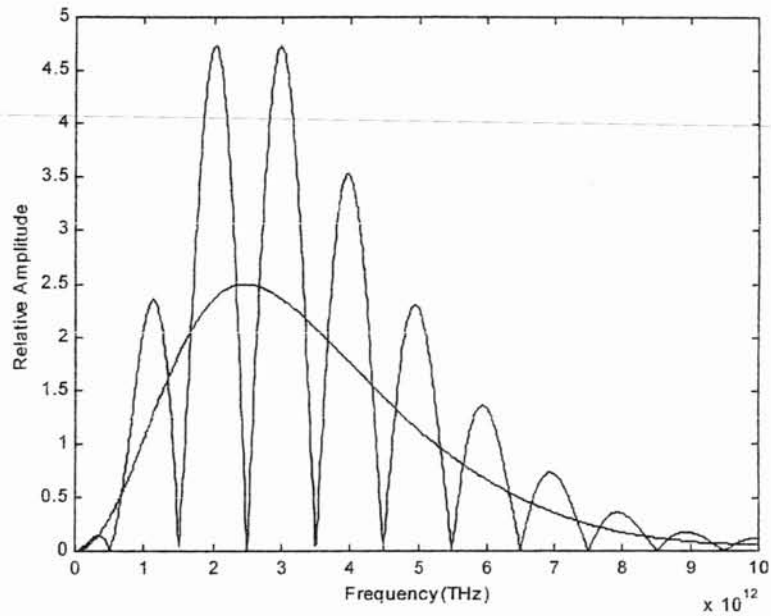


Figure 4-10 Interference due to frequency dependent phase shift (shown by solid line) over a THz pulse spectrum (dashed line)

Refractive Index & Absorption Coefficient

The measured frequency dependent signal, $E_{\text{meas}}(\omega)$ can be written as:

$$E_{\text{meas}}(\omega) = E_{\text{ref}}(\omega) + E_{\text{samp}}(\omega) \quad (4-6)$$

where $E_{\text{samp}}(\omega)$ is given by:

$$E_{\text{samp}}(\omega) = E_{\text{ref}}(\omega) \{ \exp(-ik_o [n(\omega) - 1]d + i\Phi(\omega)) \} \quad (4-7)$$

Substituting, $E_{\text{samp}}(\omega)$ in equation (4-6) gives $E_{\text{meas}}(\omega)$ as:

$$E_{\text{meas}}(\omega) = E_{\text{ref}}(\omega) \left[1 - \exp(-ik_o (n(\omega) - 1) d + i\Phi(\omega)) \right] \quad (4-8)$$

where we have assumed the index and absorption of the sample are small so that $t_{1S} \cong t_{S1} \cong 1$ [10].

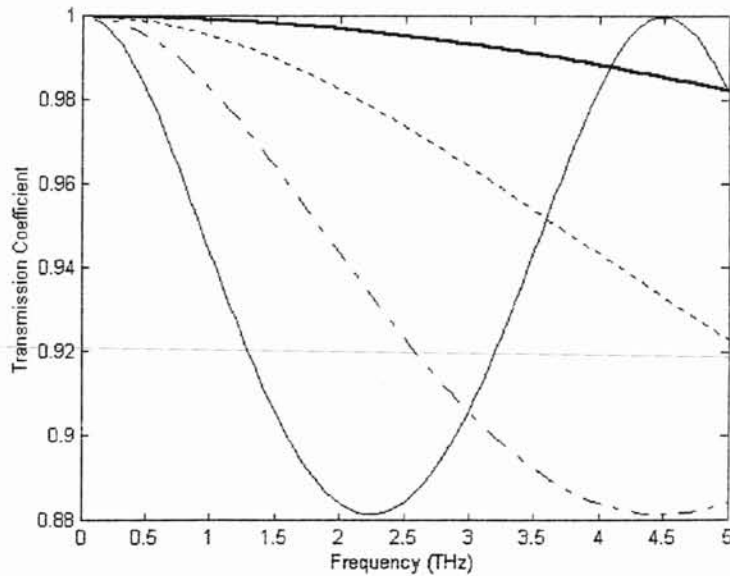


Figure 4-11. Calculated transmission Coefficients for free standing mylar sample showing Fabry-Perot oscillations. Thick solid line - $2\mu\text{m}$, Dashed line - $5\mu\text{m}$, Dashed-dot line - $10\mu\text{m}$, Thin solid line - $20\mu\text{m}$

The assumption of ignoring the Fabry-Perot terms is valid for films with a thickness-index product much less than one wavelength. This is shown in figure 4-11 which illustrates numerically calculated transmission coefficients [28] for a free standing mylar film at normal incidence for different sample thicknesses d . The index for the sample used is 1.67 which is a published value at 1GHz [31]. From this it can be seen that in the mylar film errors are less than 2% for thicknesses of $< \lambda/30$ and less than 5% for thickness of $\lambda/20$. These errors will increase for higher index films.

The phase term, $\Phi(\omega)$, accounts for both the 10.7° phase difference from that needed for destructive interference as well as a frequency dependent term accounting for small misalignments of the sample arm relative to the reference arm. $\Phi(\omega)$ is determined by taking a scan with no sample in the interferometer, (see appendix for derivation of $\Phi(\omega)$).

$$E_{\phi}(\omega) = E_{\text{ref}}(\omega)[1 - \exp(i\Phi(\omega))] \quad (4-9)$$

Measurements of the reference arm pulse, $E_{\text{ref}}(\omega)$, and the interferometer signal with, $E_{\text{meas}}(\omega)$, and without, $E_{\phi}(\omega)$, a sample permit determination of the complex refractive index (see appendix for derivation):

$$n_r(\omega) - in_i(\omega) = \frac{-i}{k_o d} \ln \left[\frac{E_{\text{meas}}(\omega) - E_{\phi}(\omega)}{E_{\phi}(\omega) - E_{\text{ref}}(\omega)} + 1 \right] + 1 \quad (4-10)$$

This measurement of the complex index can be simplified for thin samples of low index. Here $k_o(n(\omega)-1)d \ll 1$ which permits expanding the exponential in equation (4-8) as a series [10], $\exp(x) \cong 1+x$. The Taylor series expansion for $\exp(x)$ is given as:

$$\exp(x) = 1 + x + \frac{x^2}{2!} + \dots \quad -\infty < x < +\infty \quad (4-11)$$

The third term in equation (4-11) will be very small for thin samples of low index, $k_o(n(\omega)-1)d \ll 1$. So only the first two terms are being considered.

The complex index can then be calculated by dividing the measured signal by the reference when the phase shift, $\Phi(\omega)$, is known. So equation (4-8) can be written as:

$$\frac{E_{\text{meas}}(\omega)}{E_{\text{ref}}(\omega)} = 1 - \exp(-ik_o[n(\omega) - 1]d + i\Phi(\omega)) \quad (4-12)$$

The exponential term in equation (4-12) can be written as:

$$\exp(-ik_o[n(\omega) - 1]d + i\Phi(\omega)) \cong 1 + (-ik_o[n(\omega) - 1]d + i\Phi(\omega)) \quad (4-13)$$

Substituting equation (4-13) in equation (4-12), we get:

$$\frac{E_{\text{meas}}(\omega)}{E_{\text{ref}}(\omega)} \cong k_o n_i(\omega)d + ik_o[n_r(\omega) - 1]d + i\Phi(\omega) \quad (4-14)$$

Due to the superposition of THz pulses from both the reference and sample arms, the THz interferometer is less sensitive to long term fluctuations in the THz signal than standard THz-TDS. In standard THz-TDS, the determination of the complex index is difficult in the case when the term $k_o(n(\omega)-1)d$ in equation (3-1) is small. In this case, slow variations in the THz spectrum caused by laser or mechanical fluctuations can be of the same magnitude as the measured change, leading to errors in the measured complex index. To account for this experimental artifact, the drift between the sample and reference spectra is represented by a drift error term, $\Delta(\omega)$, with $\Delta(\omega)$ small such that $\exp(i\Delta(\omega)) \cong 1$. For small values of $k_o(n-1)d$ so that the exponential is represented as a series, the measured signal is (see appendix for derivation):

$$\frac{E_{\text{samp}}(\omega)e^{i\Delta(\omega)}}{E_{\text{ref}}(\omega)} \cong 1 + i \left(\Delta(\omega) - \frac{\omega}{c} (n_r(\omega) - n_i(\omega) - 1)d \right) \quad (4-15)$$

From this it is seen that in typical THz-TDS the drift error term, $\Delta(\omega)$, is additive to the measurement. Compared to standard THz-TDS, the interferometer measurement error can be found by including the drift error term in equation (4-8): (see appendix for derivation).

$$\frac{E_{\text{meas}}(\omega)e^{i\Delta(\omega)}}{E_{\text{ref}}(\omega)} \cong \Delta(\omega)\{k_o n_i(\omega)d + ik_o[n_r(\omega) - 1]d + i\Phi(\omega)\} \quad (4-16)$$

Given that $k_o(n-1)d \ll 1$, the drift error term is seen to be multiplicative with the measured values of the complex index rather than additive as above. For a magnitude of $\Delta(\omega)$ close to that of $k_o(n-1)d$, this leads to a much smaller overall error in the measurement, provided the phase shift, $\Phi(\omega)$, is known.

As illustrated above, the measured interference signal, permits direct determination of the frequency dependent complex index of the sample. The frequency dependent index, determined from equation (4-10) is shown in figure 4-12. The index of refraction, given by solid line, is close to that of the published DC dielectric constant [31], shown by the dashed line. The oscillations in the data are in part due to water vapor in the beam path [30]. The frequency dependent absorption, determined from equation (4-10) is shown in figure 4-13 which is close to zero [31]. The absorption of this thin film is not measurable since the absorption length $2\alpha L$ is $\ll 1$. The major limitation to measuring the index and absorption are due to the variable film thickness of the commercial Mylar samples of approximately $\pm 10\%$ corresponding to index uncertainties of ± 0.17 .

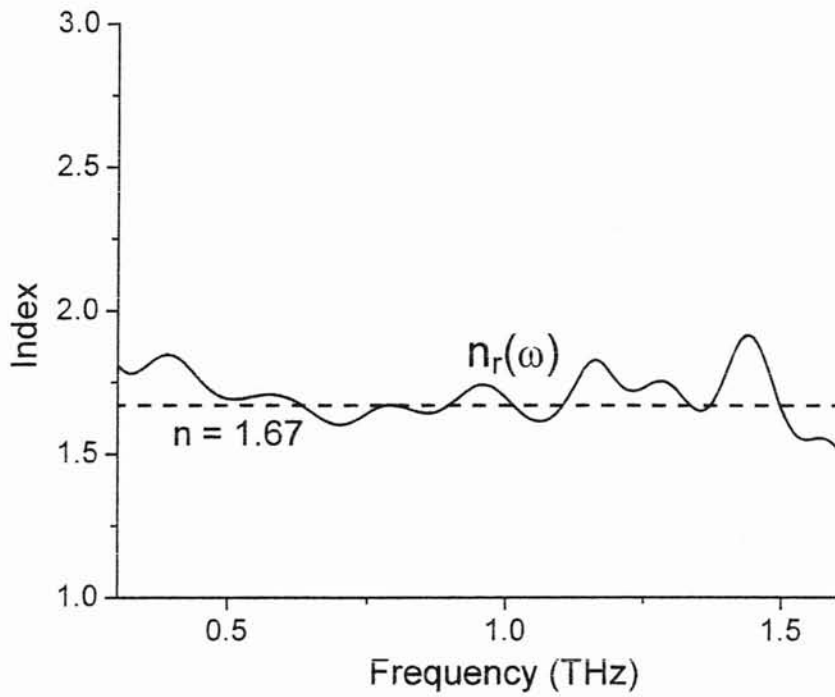


Figure 4-12 Measured real refractive index for 2 μ m thick mylar film

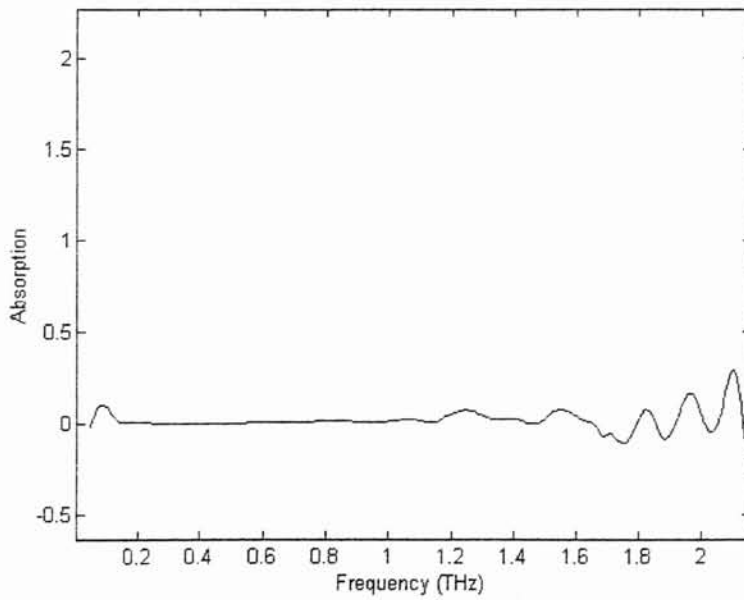


Figure 4-13 Measured absorption for 2 μ m thick mylar film

Time-domain Analysis

In some measurement applications, such as quality control, one wishes to rapidly determine changes in film thickness or index. THz interferometry is capable of determining small changes in film thickness or index directly from the time domain data without measurement of the full THz pulse. The effect of a film of index, $n = n_0 + \Delta n(\omega)$ with $\Delta n(\omega) \ll n_0$ and $\alpha L \ll 1$, and thickness, d , is to shift the THz pulse in time by an amount $\Delta t = d(n-1)/c$ for a single pass of the THz pulse through the film and $\Delta t = 2d(n_r-1)/c$ for a double pass. In this case, with no sample in the beam, the measured electric field in the reference arm given by $E_{ref}(t)$ and that of the sample arm $E_{samp}(t) = -E_{ref}(t) + E_{\Phi}(t)$, where $E_{\Phi}(t)$ is the small residual time signal due to the phase shift, $\Phi(\omega)$. Inserting the sample shifts the pulse in the sample arm an amount Δt . With the time shift, the measured signal is $E_{meas}(t) \cong E_{ref}(t) - E_{ref}(t - \Delta t) + E_{\Phi}(t)$. With the known $E_{\Phi}(t)$ subtracted from the data, the time shifted reference pulse can be expanded in a Taylor series with only the first order terms being retained for small Δt . In this case:

$$E_{meas}(t) = E_{ref}(t) - E_{ref}(t - \Delta t) \cong \Delta t E_{ref}'(t) \quad (4-17)$$

where the prime corresponds to the time derivative (see appendix for derivation). The quantity $\Delta t = d(n-1)/c$ can be determined by numerically integrating $E_{meas}(t)$ and determining Δt by a comparison to the known reference pulse. Since the reference pulse shape is constant, for values of Δt small compared with the maximum frequency component of the THz pulse the film thickness-index product given through Δt is directly proportional to the size of the measured signal, $E_{meas}(t)$, from the THz interferometer.

To demonstrate the measurement sensitivity of the interferometer we measure free standing films of nominally 2 μm thick films of DuPont type C Mylar® polyester film [31]. Mylar is a flexible composite composed of non-woven polyester fiber mat and polyester film, laminated with a high temperature polyester adhesive system and 100% filled with resin, providing a smooth varnish like surface. Typical application for mylar films is its use as a dielectric for metalized/film/foil capacitors. The thickness was independently measured at several points on the sample using the white light transmission spectra and comparing to that calculated for a thin film. The thickness was found to be $2.15 \pm 0.2 \mu\text{m}$. The film, stretched taut to eliminate wrinkles, was mounted on a frame placed in the sample arm of the interferometer. Measurement of the refractive index-thickness product of the Mylar® film extracted directly from the time domain data utilizing equation (4-17) are given in figure 4-14 from the data shown in figure 4-4 and 4-6. To find the film thickness, $E_{\phi}(t)$ is subtracted from the measured data of figure 4-6, then integrated and a value of Δt is found which when multiplied by the integrated data will return the reference pulse shape. The reference pulse is shown as a solid line in figure 4-14 with the fit (points) of the Mylar® films using a value of Δt of 10.5 fs, corresponding to $2d(n_r-1)$ of 3.15 μm . Using the published 1 GHz dielectric constant of $(n_r)^2 = \epsilon_r = 2.8$ [31] this returns a value of $d = 2.3 \mu\text{m}$ which agrees with the measured film thickness.

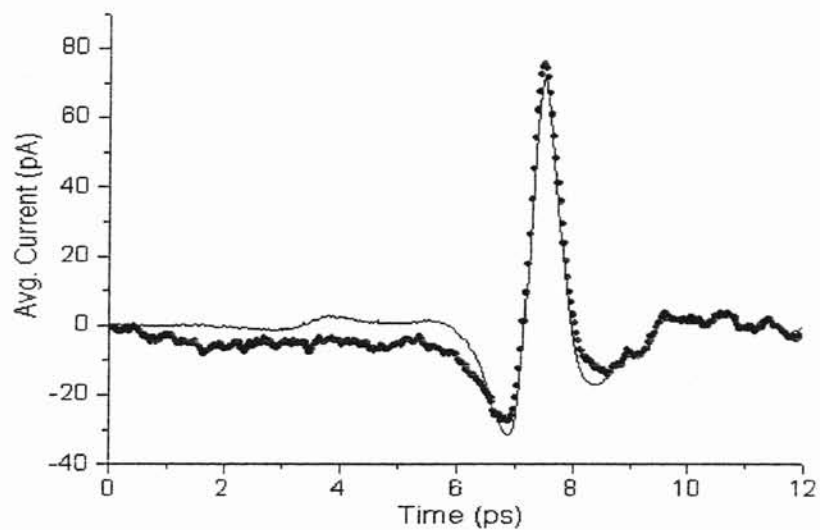


Figure 4-14 Measured reference pulse(solid line) and the fit of the measured pulse(dotted line) with background phase subtracted following equation (4-17) with Δt of 10.5 fs.

B. Retroreflector Configuration

Experimental setup

The experimental setup shown in figure 4-13 is the modification of the silicon prism configuration (figure 4-4) where the two silicon prisms in the reference and sample arms are replaced by retroreflectors (50x50 mm), single 1mm thick and 4 inches diameter silicon beam splitter is used instead of two silicon beamsplitters and linear polarizer is placed in front of the receiver.

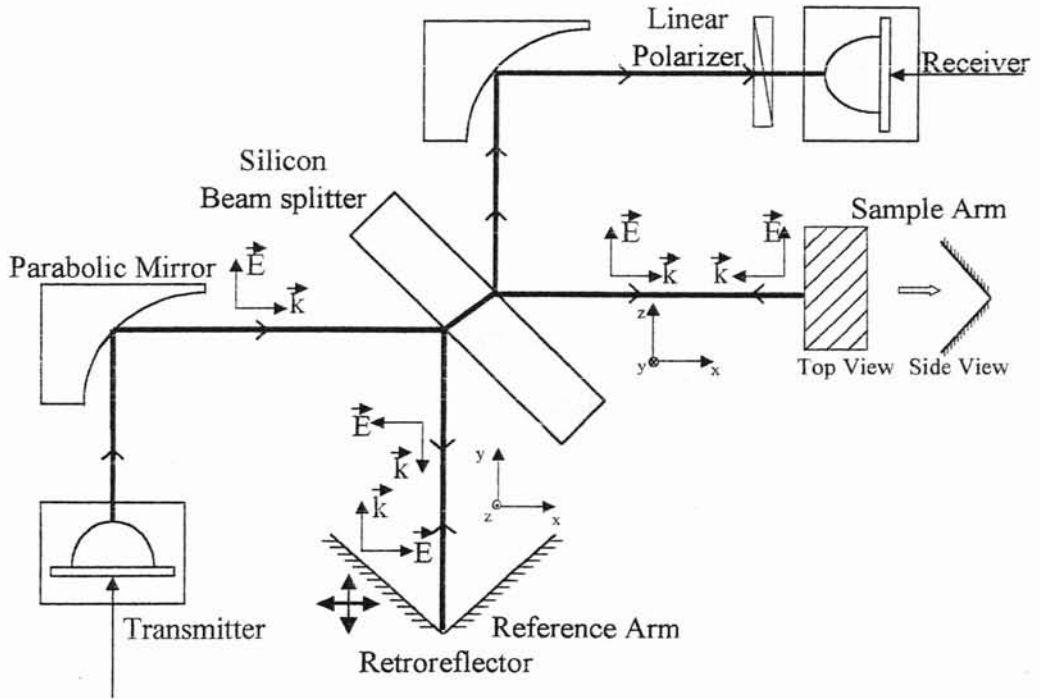


Figure 4-15. THz Interferometer, Retroreflector Configuration with Michelson Setup

The sample arm retroreflector is oriented 90° perpendicular to the plane of propagation with respect to the reference arm retroreflector. All the controls used to get full position and angle control of the beams in the reference and sample arms are similar to silicon prism configuration except the sample arm is translated vertically (out of page) to get independent position control.

Experimental Results

The measured pulses in the reference arm, $E_{\text{ref}}(t)$, and sample arm, $E_{\text{samp}}(t)$, obtained by blocking one arm and measuring the signal in the other arm are shown in figure 4-14(a). The reference arm signal is shown by the solid line and the sample arm signal is shown by the dashed line. The nearly 180° phase shift of the reference arm relative to the sample arm is clearly seen. Also the peak signal is about 135 pA where as it is only 70 pA with silicon prism configuration.

Figure 4-14(b) shows the measured interferometer signal with both sample and reference arms open. The measured peak to peak signal here is 2 % of the difference between the peaks of the reference and sample arms measured individually. In order to get complete destructive interference between the sample and reference arm signals, the THz signal should be radially symmetric which will provide good spatial overlap [32] between the two signals. The slight misalignments of the THz signal should also be considered. This is roughly 57 % improvement as compared with the silicon prism configuration.

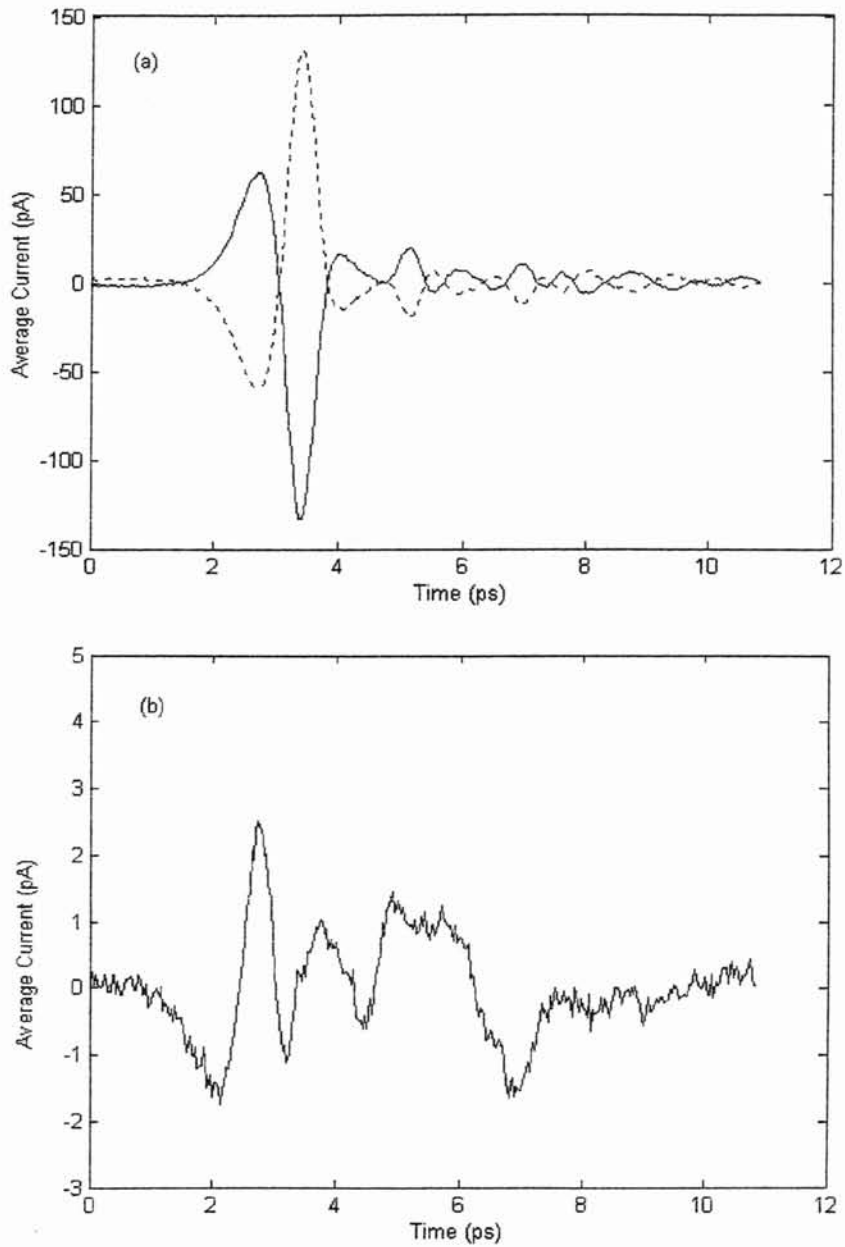


Figure 4-16 Measurements of the THz Interferometer signals, Retroreflector Configuration. (a) Only one arm open, dashed line – reference arm signal, solid line – sample arm signal. (b) Both arms open

Figure 4-17 shows the interferometer signals with both arms open. The solid line is without the sample which is taken by placing two identical silicon wafers as substrates in both the reference and sample arms in the figure 4-14. The dashed line is with 300 nm thick layer of silicon dioxide grown as a sample in the sample arm substrate using thermal furnace.

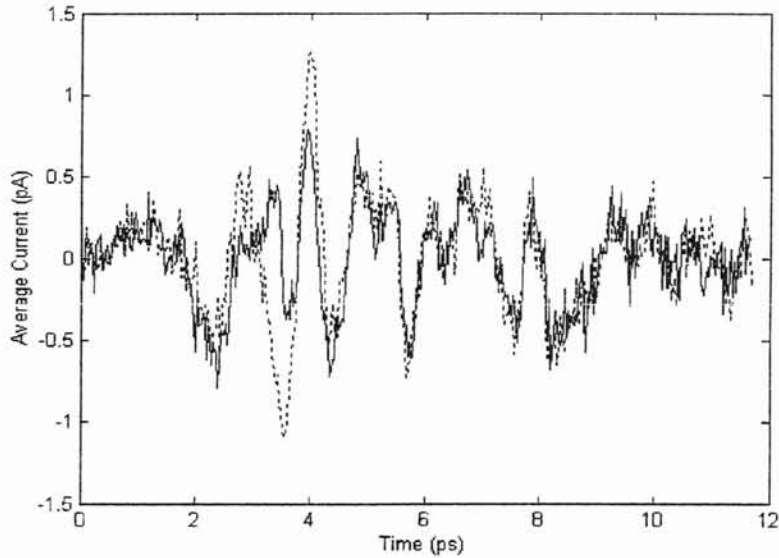


Figure 4-17 Interferometer signals with both arms open, solid line - without sample, dashed line – with 300 nm thick layer of silicon dioxide as a sample.

The thermal furnace conditions to grow 300 nm thick layer of silicon dioxide are: temperature - 1100°C, atmosphere – steam, duration – 15 minutes. A violet blue color should be observed for 300nm thickness growth. As shown in figure 4-18, the silicon dioxide growth will be 54% above the substrate and 46% below the substrate.

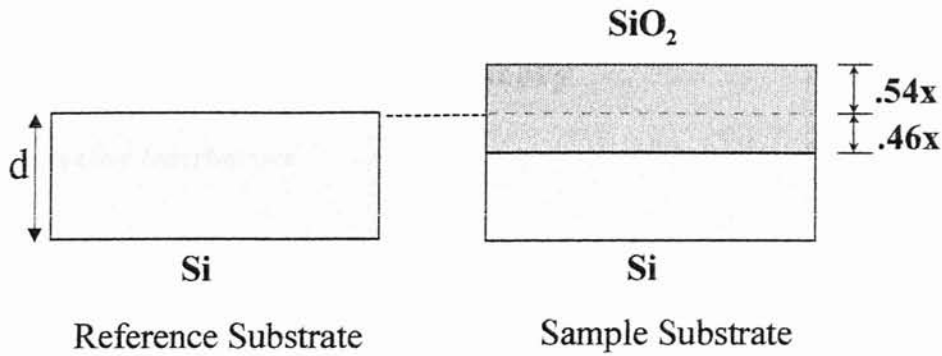


Figure 4-18 Silicon dioxide growth in the Silicon wafer, d – Si substrate thickness, x – Silicon dioxide thickness.

According to the figure 4-18, the shift in time for the double pass of the THz pulse in the reference and sample substrates are given as follows:

For reference substrate, $\Delta t = 2d(n_{\text{si}}-1)/c$ where n_{si} is the silicon index and for sample substrate, $\Delta t = 2[(d-0.46x)n_{\text{si}} + (0.54x) n_{\text{ox}}] /c$ where n_{ox} is the silicon dioxide index. By substituting the values, $n_{\text{si}} = 3.42$ and $n_{\text{ox}} = 2$, we get the time shift for the interferometer signal with both arms open to be, $\Delta t = -0.99x$. In other words growth of an oxide layer of thickness x will shift the THz pulse earlier in time by an amount equal to the free space propagation time of the film thickness, or in the case of the oxide layers illustrated here, a corresponding delay in time of approximately 2 fs.

Theory

Destructive Interference

The frequency dependent fields for the reference, $E_{\text{ref}}(\omega)$ and sample, $E_{\text{samp}}(\omega)$ arms are given by the field input into each arm, $E_o(\omega)$, modified by the fresnel transmission and reflection coefficients for the surface normals shown in figure 4-15. By assuming the paraboloidal reflectors to be flat metal mirrors and the index for both the paraboloidal and retroreflectors to be a large number, $E_{\text{ref}}(\omega) = -0.375E_o(\omega)$ and $E_{\text{samp}}(\omega) = +0.375E_o(\omega)$. This phase shift is due to the polarization difference between the two arms. When the input electric field is polarized in the plane of incidence (P) [28], according to the reference arm configuration, the field undergoes (S) polarization where as the sample arm does not undergo any change in polarization.

Refractive Index & Absorption Coefficient

For the interferometer shown in figure 4-15, the measured frequency dependent signal, $E_{\text{ref}}(\omega) + E_{\text{samp}}(\omega)$ can be written as :

$$E_{\text{meas}}(\omega) = E_{\text{ref}}(\omega) \left[1 - \exp(-ik_o(n(\omega) - 1)d + i\Phi(\omega)) \right]$$

where it is assumed that the index and absorption of the free standing sample, d are small so that $t_{1S} \cong t_{S1} \cong 1$ [10]. Here the phase term, $\Phi(\omega)$, accounts for small misalignments of the sample arm relative to the reference arm.

The derivation of complex refractive index from the measured signal for the retroreflector configuration is same as that of the silicon prism configuration which is given by the equation (4-10)

$$n_r(\omega) - in_i(\omega) = \frac{-i}{k_0 d} \ln \left[\frac{E_{\text{meas}}(\omega) - E_{\Phi}(\omega)}{E_{\Phi}(\omega) - E_{\text{ref}}(\omega)} + 1 \right] + 1$$

CHAPTER V

CONCLUSIONS

In this study, a THz interferometer is developed based on the Michelson configuration which can perform characterization of thin, low absorbance samples. This device utilizes a geometry which incorporates a nearly 180° phase shift in one arm to produce destructive interference canceling laser noise and drift. So the system automatically compensates for changes in the THz signal over the course of a measurement and hence accuracy is improved compared to standard THz-TDS.

Two different configurations of interferometer setups have been developed to achieve the 180° phase shift of one arm relative to the other for destructive interference. The first approach was using high resistivity silicon prisms where total internal reflection of THz pulses provides a nearly 180° phase shift. Due to the constant and frequency independent phase difference of 10.7° present between the reference and sample arm signals even under optimal alignment conditions complete destructive interference was not possible to achieve.

The second approach was using retroreflectors where polarization difference of THz pulses provides nearly 180° phase shift. With the retroreflector configuration the measured peak to peak signal for the destructive interference is 2 % of the difference between the peaks of the reference and sample arms measured individually where as it is 3.5 % with the silicon prism configuration. In order to get complete destructive

interference between the sample and reference arm signals, the THz signal should be radially symmetric which will provide good spatial overlap between the two signals. The slight misalignments of the THz signal should also be considered. This is roughly 57 % improvement as compared with the silicon prism configuration.

Characterization of 2 μm thick mylar film has been demonstrated with silicon prism configuration. The index of the mylar film measured is 1.67 which is close to the published value at 1GHz. The measured absorption of the thin film is close to zero. The thickness of the sample measured is 2.3 μm which is obtained directly from the time domain data and it is close to the variable film thickness of $\pm 10\%$ of 2.3 μm .

CHAPTER VI

REFERENCES

1. A. Ulman, "Characterization of Organic Thin Films", Butterworth-Heineman, Boston,(1995).
2. F. L. McCrackin and J. P. Colson, "Ellipsometry in the Measurement of Thin Films" (E. Passaglia, R. R. Stromberg, and J. Kruger, Eds), National Bureau of Standards Misc. Publ. 256, Washington DC, (1964).
3. Pramod K. Rastogi, "Optical Measurement Techniques and Applications", ArtechHouse Inc., Boston, (1997).
4. D. Grischkowsky, S. Keiding, M. van Exter, and C. Fattinger, "Far-infrared time-domain spectroscopy with terahertz beams of dielectrics and semiconductors", Journal of Optical Society of America B, Vol. 7, No. 10, 2006-2015, (1990).
5. D. M. Mittleman, S. Hunsche, L. Boivin, and M.C. Nuss, "T-ray tomography", Optics Letters, Vol. 20, No. 12, 904-906, (1997).
6. D. M. Mittleman, R. H. Jacobson, and M.C. Nuss, "T-Ray Imaging", IEEE Journal of Selected Topics in Quantum Electronics, Vol.2, No.3, 679-692, (1996).
7. R. A. Cheville and D. Grischkowsky, "Far-infrared terahertz time-domain spectroscopy of flames", Optics Letters, Vol. 20, No. 15, 1646-1648, (1995).

8. V. Grebenev, E. Knoesel, and L. Bartels, "Destructive Interference of freely propagating terahertz pulses and its potential for high-resolution spectroscopy and optical computing", *Applied Physics Letters*, Vol. 79, No. 2, 145-147, (2001).
9. M. Ree, K. -J. Chen, D. P. Kirby, N. Katzenellenbogen, and D. Grischkowsky, "Anisotropic properties of high-temperature polyimide thin films: Dielectric and thermal-expansion behaviors", *Journal of Applied Physics*, Vol. 72, No. 5, 2014-2021, (1992).
10. Z. P. Jiang, M. Li, and X.C. Zhang, Dielectric constant measurement of thin films by differential time-domain spectroscopy", *Applied Physics Letters*, Vol. 76, No.22, 3221-3223, (2000).
11. J. L. Johnson, T. D. Dorney, and D. M. Mittleman, "Enhanced depth resolution in terahertz imaging using phase-shift interferometry", *Applied Physics Letters*, Vol. 78, No. 6, 835-837, (2001).
12. A. B. Ruffin, J. V. Rudd, J. F. Whitaker, S. Feng, and H. G. Winful, " Direct observation of the gouy phase shift with single-cycle terahertz pulses", *Physical Review Letters*", Vol. 83, No. 17, 3410-3413, (1999).
13. S. Krishnamurthy, M. T. Reiten, S.A. Harmon, and R. A. Cheville, Characterization of thin polymer films using terahertz time-domain interferometry", *Applied Physics Letters*, Vol. 79, No. 6, 875-877, (2001).
14. S. Tolansky, "An introduction to Interferometry", Halsted Press, Second Edition, (1973).
15. Edward Collett, " Mathematical Formulation of the interference laws of Fresnel and Arago", *American Journal of Physics*, Vol. 39, 1483-1495, (1971).

16. Richard Barakat, "Analytic proofs of the Arago-Fresnel laws for the interference of polarized light", *Journal of Optical Society of America B*, Vol. 10, No. 1, 180-185, (1993).
17. W. Ewart Williams, "Applications of interferometry", John Wiley & Sons Inc., Fourth Edition, (1950).
18. P. Hariharan, "Basics of interferometry", Academic Press, (1992).
19. Brian C. Smith, "Fundamentals of Fourier transform infrared spectroscopy", CRC Press, (1996).
20. Peter R. Griffiths and James A. de Haseth, "Fourier transform infrared spectrometry", John Wiley & Sons, (1986).
21. N. Katzenellenbogen and D. Grischkowsky, "Efficient generation of 380 fs pulses of THz radiation by ultrafast laser pulse excitation of a biased metal-semiconductor interface", *Applied Physics Letters*, Vol. 58, No. 3, 222-224, (1991).
22. T. I. Jeon and D. Grischkowsky, "Characterization of optically dense, doped semiconductors by reflection THz time-domain spectroscopy", *Applied Physics Letters*, Vol. 72, No. 23, 3032-3034, (1998).
23. T. I. Jeon, D. Grischkowsky, A. K. Mukherjee, and Reghu Menon, "Electrical characterization of conducting polypyrrole by THz time-domain spectroscopy", *Applied Physics Letters*, Vol. 77, No. 16, 2452-2454, (2000).
24. Tae-in Jeon, "New applications of THz time-domain spectroscopy", Thesis, Oklahoma State University, (1997).

25. M. van Exter and D. Grischkowsky, "Characterization of an optoelectronic terahertz beam system", IEEE transactions on microwave theory and techniques, Vol. 38, No.11, 1684-1691, (1990).
26. DSP Lock-in-Amplifier, "Model SR830", Stanford Research Systems Inc. California, (1993).
27. High Voltage Amplifier, "Model 610 D", Trek Inc., New York, (2000).
28. M. Born and E. Wolf, "Principles of Optics", 7 ed., Cambridge University Press, New York, (1999).
29. S. R. Keiding and D. Grischkowsky, "Measurements of the phase shift and reshaping of terahertz pulses due to total internal reflection", Optics Letters, Vol. 15, No. 1, 48-50, (1990).
30. M. van Exter, Ch. Fattinger, and D. Grischkowsky, "Terahertz time-domain spectroscopy of water vapor", Optics Letters, Vol. 14, No. 20, 1128-1130, (1989).
31. Dupont Teijin Films, "Mylar polyester film electrical properties", Dupont Teijin Films, Wilmington, DE, (1995).
32. M. T. Reiten, S. A. Harmon, R.A. Cheville, "THz beam propagation measured through 3D amplitude profile determination", To be Published.

APPENDIX

Derivation for the phase term $\Phi(\omega)$

$\Phi(\omega)$ is determined by taking a scan with no sample in the interferometer, so $E_{\Phi}(\omega)$ is written as:

$$E_{\Phi}(\omega) = E_{\text{ref}}(\omega)[1 - \exp(i\Phi(\omega))]$$
$$\frac{E_{\Phi}(\omega)}{E_{\text{ref}}(\omega)} = 1 - \exp(i\Phi(\omega)) \quad (\text{A-1})$$

By taking logarithm on both sides of equation (A-1), $\Phi(\omega)$ is given by:

$$\Phi(\omega) = -i \ln \left(1 - \frac{E_{\Phi}(\omega)}{E_{\text{ref}}(\omega)} \right)$$

Derivation for complex refractive index

Equation (4-8) can be written as:

$$\exp(-ik_0[n(\omega) - 1]d) * \exp(i\Phi(\omega)) = 1 - \frac{E_{\text{meas}}(\omega)}{E_{\text{ref}}(\omega)} \quad (\text{A-2})$$

Substituting the value of $\Phi(\omega)$ and taking logarithm on both sides of the equation (A-2), is written as:

$$-ik_0[n(\omega) - 1]d = \frac{\ln \left(1 - \frac{E_{\text{meas}}(\omega)}{E_{\text{ref}}(\omega)} \right)}{\ln \left(1 - \frac{E_{\Phi}(\omega)}{E_{\text{ref}}(\omega)} \right)} \quad (\text{A-3})$$

Solving for complex refractive index, $n(\omega)$ from equation (A-3), we get

$$n_r(\omega) - in_i(\omega) = \frac{-i}{k_o d} \ln \left[\frac{E_{\text{meas}}(\omega) - E_{\Phi}(\omega)}{E_{\Phi}(\omega) - E_{\text{ref}}(\omega)} + 1 \right] + 1$$

Comparison of regular THz-TDS with THz interferometer

In THz -TDS setup equation (3-1) can be written as:

$$\frac{E_{\text{samp}}(\omega)}{E_{\text{ref}}(\omega)} = \exp(-ik_o[n(\omega) - 1]d) \quad (\text{A-4})$$

By including a drift error term, $\Delta(\omega)$ so that $\exp(i\Delta(\omega)) \cong 1$ in equation (A-4), is written as:

$$\frac{E_{\text{samp}}(\omega) \exp(i\Delta(\omega))}{E_{\text{ref}}(\omega)} = \exp\{-ik_o[n(\omega) - 1]d + i\Delta(\omega)\} \quad (\text{A-5})$$

The exponential term in equation (A-5) is written as:

$$\exp\{-ik_o[n(\omega) - 1]d + i\Delta(\omega)\} \cong 1 + (-ik_o[n(\omega) - 1]d + i\Delta(\omega)) \quad (\text{A-6})$$

Since, $k_o(n(\omega)-1)d \ll 1$ only first two terms are being considered for the exponential term.

Substituting equation (A-6) in equation (A-5), we get,

$$\frac{E_{\text{samp}}(\omega) e^{i\Delta(\omega)}}{E_{\text{ref}}(\omega)} \cong 1 + i \left(\Delta(\omega) - \frac{\omega}{c} (n_r(\omega) - in_i(\omega) - 1) d \right)$$

In THz interferometer setup equation (4-16) can be written as:

$$\frac{E_{\text{meas}}(\omega)}{E_{\text{ref}}(\omega)} = 1 - \exp(-ik_o[n(\omega) - 1]d + i\Phi(\omega)) \quad (\text{A-7})$$

By including a drift error term, $\Delta(\omega)$ so that $\exp(i\Delta(\omega)) \cong 1$ in equation (A-7), is written

as:

$$\frac{E_{\text{meas}}(\omega)e^{i\Delta(\omega)}}{E_{\text{ref}}(\omega)} = \{1 - \exp(-ik_o[n(\omega) - 1]d + i\Phi(\omega))\} \exp(i\Delta(\omega)) \quad (\text{A-8})$$

The exponential term $\exp(-ik_o[n(\omega) - 1]d + i\Phi(\omega))$ in equation (A-8) is written as:

$$\exp(-ik_o[n(\omega) - 1]d + i\Phi(\omega)) \cong 1 + (-ik_o[n(\omega) - 1]d + i\Phi(\omega)) \quad (\text{A-9})$$

Since, $k_o(n(\omega)-1)d \ll 1$ only first two terms are being considered for the exponential term

Substituting equation (A-9) in equation (A-8), we get,

$$\frac{E_{\text{meas}}(\omega)e^{i\Delta(\omega)}}{E_{\text{ref}}(\omega)} \cong \Delta(\omega) \{k_o n_i(\omega)d + ik_o[n_r(\omega) - 1]d + i\Phi(\omega)\}$$

Time domain analysis

The Taylor series for $f(x)$ about $x = a$ are defined as the following equations:

$$f(x) = f(a) + f'(a)(x - a) + \frac{f''(a)(x - a)^2}{2!} + \dots \quad (\text{A-10})$$

$$f(x - h) = f(x) - hf'(x) + \frac{h^2}{2!} f''(x) + \dots \quad (\text{A-11})$$

Subtracting $f(x-h)$ from $f(x)$ gives:

$$f(x) - f(x - h) \cong hf'(x) - \frac{h^2}{2!} f''(x) + \dots \quad (\text{A-12})$$

According to equation (A-11), $E_{\text{ref}}(t - \Delta t)$ can be written as:

$$E_{\text{ref}}(t - \Delta t) = E_{\text{ref}}(t) - \Delta t E_{\text{ref}}'(t) + \dots$$

According to equation (A-12), $E_{\text{ref}}(t) - E_{\text{ref}}(t - \Delta t)$ can be written as:

$$E_{\text{ref}}(t) - E_{\text{ref}}(t - \Delta t) \cong \Delta t E_{\text{ref}}'(t)$$

And finally, $E_{\text{meas}}(t) = E_{\text{ref}}(t) - E_{\text{ref}}(t - \Delta t) \cong \Delta t E_{\text{ref}}'(t)$

VITA 2

Sailaja Krishnamurthy

Candidate for the Degree of
Master of Science

Thesis: TERAHERTZ INTERFEROMETER FOR CHARACTERIZATION OF THIN FILM SAMPLES

Major Field: Electrical Engineering

Biographical:

Personal Data: Born in Tiruttani, Tamil Nadu, India on 10th June 1974, the daughter of Ramachandra Raju and Nirmala.

Education: Graduated from Government Higher Secondary School, Tiruttani, Tamil Nadu, India, in April 1989; received polytechnic diploma in Electronics & Communication Engineering from Government Polytechnic Institute for women, Taramani, Madras, India, in May 1992; completed Bachelor of Science in Electrical Engineering from University of Madras, Madras, India, in April 1997, completed the requirements for the Master of Science degree at Oklahoma State University in August 2002.

Experience: Employed in Revelation Engineering, Bozeman, Montana, as an Electrical Engineer from November 1999 to May 2000; employed by Oklahoma State University, School of Electrical and Computer Engineering as a research assistant from August 2000 to present.

Professional Memberships: The Institute of Electrical and Electronics Engineers.